The Extratropical Transition of Hurricane Debby (1982) and the Subsequent Development of an Intense Windstorm over Finland

TERHI K. LAURILA

Finnish Meteorological Institute, Helsinki, Finland

VICTORIA A. SINCLAIR

Institute for Atmospheric and Earth System Research/Physics, Faculty of Science, University of Helsinki, Helsinki, Finland

HILPPA GREGOW

Finnish Meteorological Institute, Helsinki, Finland

ABSTRACT

On 22 September 1982, an intense windstorm caused considerable damage in northern Finland. Local forecasters noted that this windstorm potentially was related to Hurricane Debby, a category 4 hurricane that occurred just 5 days earlier. Due to the unique nature of the event and lack of prior research, our aim is to document the synoptic sequence of events related to this storm using ERA-Interim reanalysis data, best track data, and output from OpenIFS simulations. During extratropical transition, the outflow from Debby resulted in a ridge building and an acceleration of the jet. Debby did not reintensify immediately in the midlatitudes despite the presence of an upper-level trough. Instead, ex-Debby propagated rapidly across the Atlantic as a diabatic Rossby wave–like feature. Simultaneously, an upper-level trough approached from the northeast and once ex-Debby moved ahead of this feature near the United Kingdom, rapid reintensification began. All OpenIFS forecasts diverged from reanalysis after only 2 days indicating intrinsic low predictability and strong sensitivities. Phasing between Hurricane Debby and the weak trough, and phasing of the upper- and lower-level potential vorticity anomalies near the United Kingdom was important in the evolution of ex-Debby. In the only OpenIFS simulation to correctly capture the phasing over the United Kingdom, stronger wind gusts were simulated over northern Finland than in any other simulation. Turbulent mixing behind the cold front, and convectively driven downdrafts in the warm sector, enhanced the wind gusts over Finland. To further improve understanding of this case, we suggest conducting research using an ensemble approach.

1. Introduction

On 22 September 1982, an intense windstorm affected northern Finland causing two fatalities and significant damage to forests destroying three million cubic meters of timber. The storm, which was given the name Mauri, is one of the most intense windstorms Finland has experienced. Windstorms in northern Europe and Finland are primarily caused by extratropical cyclones that have their genesis regions in the midlatitudes and develop due to baroclinic instability (Hoskins and Hodges 2002; Zappa et al. 2013). However, it was argued back in 1982 that Mauri was caused by the remnants of a category 4 hurricane, Debby, which had undergone extratropical transition (ET).

In the North Atlantic, almost half of hurricanes undergo ET; a process where a tropical cyclone transforms into an extratropical cyclone due to entering the midlatitude environment (Hart and Evans 2001; Jones et al. 2003; Evans et al. 2017). Tropical cyclones that undergo ET can occasionally lead to severe weather along the east coast of the United States and Canada (e.g., Palmén 1958; Ma et al. 2003; Galarneau et al. 2013) but there

---

are also cases that have caused damage in Europe. For example, Hurricane Iris in 1995 became extratropical and its remnants reached northwest Europe (Thorncroft and Jones 2000) whereas Hurricane Lili underwent ET in October 1996 and then passed over the United Kingdom leading to heavy rain and strong wind gusts (Browning et al. 1998; Agustí-Panareda et al. 2005). More recently, in 2017, Hurricane Ophelia transitioned into an extratropical system and its hurricane-force winds caused significant damage in Ireland and the United Kingdom and three fatalities (Stewart 2018). However, it is rare that transitioned cyclones result in high-impact events in Fenno-Scandinavia. Thus, if storm Mauri did originate from Hurricane Debby it would be a unique storm. Despite this, and that Mauri is a well-known event in Finland, no in-depth dynamic study has yet been performed about Mauri.

During the ET process, the structural characteristics of the cyclone change. The cyclone transforms from being a symmetric, warm core cyclone to an asymmetric, cold core cyclone, and the spatial extent of the cloud and precipitation increases and fronts become evident (e.g., Klein et al. 2000; Hart and Evans 2001). The vertical structure of the potential vorticity (PV) field associated with the cyclone also undergoes notable changes during ET. In general, when the cyclone is tropical, a positive PV anomaly associated with latent heating is evident in the center of the cyclone (as a vertical "PV tower") (e.g., Hoskins et al. 1985; Jones et al. 2003). After ET, the PV structure of the cyclone is typically characterized by an upper-level positive PV anomaly that is tilted westward with height (e.g., Hoskins et al. 1985; Jones et al. 2003). A transitioned cyclone can then directly interact with an upper-level trough and reintensify (Evans et al. 2017). The upper-level PV anomaly of a preexisting trough might lead to a strong reintensification of the transitioned cyclone, however the phasing between these two systems is critical in determining whether or not reintensification will occur (Ritchie and Elsberry 2007). Scheck et al. (2011) developed the concept of bifurcation points to highlight that a track bifurcation can occur when a small change in one aspect of the flow (e.g., the midlatitude trough) can result in significant changes to the subsequent circulation. In an idealized modeling study, Riemer and Jones (2014) identified a bifurcation (stagnation) point at the base of the midlatitude upstream trough that governs the bifurcation of cyclone tracks into a regime where ET occurs and another when no ET occurs.

A tropical cyclone can also affect midlatitudes by directly modulating the downstream flow [see section 2a

of Keller et al. (2019) for an overview]. This typically manifests as ridge building poleward and downstream of the transitioning tropical cyclone, downstream trough amplification, and jet streak modifications. These features have all been identified in idealized experiments (Riemer et al. 2008) and in a climatological study by Archambault et al. (2013) where time-lagged composites of the midlatitude flow were created. A case study of Hurricane Irene by Agustí-Panareda et al. (2004) highlighted that diabatically produced low-PV air at upper levels can be advected by the divergent outflow of a tropical cyclone leading to both ridge amplification and, by the subsequent steepening of the tropopause, an acceleration of the upper-level jet downstream. Similar results were also obtained more recently by Grams et al. (2013) for Typhoon Jangmi in which diabatic PV reduction at upper levels and the advection of low-PV air toward a jet streak by the tropical cyclone outflow resulted in weak ridge building. Furthermore, the impact of the transition of an extratropical cyclone on the midlatitude flow can also be transmitted farther downstream by modifying Rossby wave packets and leading to the development of new cyclones and anticyclones downstream (Riemer et al. 2008; Archambault et al. 2013). As an example, Supertyphoon Nuri (2014) amplified the downstream ridge–trough couplet that then resulted in a new cyclone developing farther downstream, amplifying the upper-level wave pattern even more and resulting in a heat wave and a cold air outbreak far downstream from the transitioned ex-Nuri (Keller et al. 2019).

In addition to direct interaction and downstream development, a less common way for a transitioned cyclone to regenerate and travel in the midlatitudes is as a diabatic Rossby wave (DRW). A DRW is a positive low-level PV anomaly embedded in a baroclinic and moist environment. Downstream of the vortex center, where poleward winds are present, isentropic ascent is induced, which leads to condensation and diabatic heating (e.g., Parker and Thorpe 1995; Moore and Montgomery 2004, 2005). Beneath the localized diabatic heating, there is a positive PV tendency, which generates positive PV downstream of the original position of the DRW. Thus, the DRW can maintain itself by this constant diabatic PV generation (Moore and Montgomery 2004). If a rapidly propagating DRW interacts with an upper-level trough it can result in an explosive intensification of the cyclone (Boettcher and Wernli 2013). Boettcher and Wernli (2013) developed an algorithm to objectively identify DRWs which states that a DRW must have the following characteristics: a closed sea level pressure contour, a positive low-level PV anomaly, substantial low-level baroclinicity, fast propagation, sufficient

moisture, and very weak upper-level forcing. An example case in which a DRW played an essential role was storm Lothar in 1999 where a positive low-level PV anomaly moved rapidly across the North Atlantic and intensified to become a damaging windstorm over Europe (Wernli et al. 2002).

In meteorological case studies, the evaluation of the synoptic-scale weather patterns is generally analyzed by using reanalysis datasets (e.g., Schenkel and Hart 2012; Hewson and Neu 2015). However, the relatively coarse resolution of most reanalysis datasets can result in small-scale cyclones, such as mesocyclones or polar lows, being completely absent or resolved but with intensities that are much weaker than observed (e.g., Uotila et al. 2009; Laffineur et al. 2014; Pezza et al. 2016). In addition, too low spatial resolution decreases the maximum wind speed and intensity of windstorms whereas too low temporal resolution may shift the location of the windstorm maximum impacts (Gregow 2013; Jokinen et al. 2014). Thus, in this study a reanalysis dataset is used only for examining the general synoptic-scale evolution whereas higher-resolution numerical simulations are employed to investigate the mesoscale features of storm Mauri.

The aims of this study are to 1) conduct a detailed analysis of the synoptic and dynamic evolution of Debby and Mauri, and 2) identify the reasons for the damaging winds over Finland on 22 September 1982. The data, model, and additional datasets used in this study are presented in section 2 and the analysis methods applied are described in section 3. Section 4 introduces the case with a brief synoptic overview based on ERA-Interim reanalysis and more in-depth analysis based on OpenIFS model simulations is presented in section 5. The conclusions are given in section 6.

2. Data, model simulations, and additional datasets

a. ERA-Interim reanalysis data

To give a general overview of this historic weather event, we use ERA-Interim reanalysis data from the European Centre for Medium-Range Weather Forecasts (ECMWF). ERA-Interim covers the years from 1979 onward, has a spatial resolution of approximately 80 km (T255 in spectral space) and there are 60 non-uniformly spaced levels with the model top at 0.1 hPa (Dee et al. 2011). The temporal resolution of the analysis fields is six hours. ERA-Interim uses a four-dimensional variational (4D-Var) data assimilation system. The limited spatial and temporal resolution of the analysis (6 h) and forecast (3 h) fields from

ERA-Interim means that ERA-Interim alone cannot be used to fully understand the dynamic evolution of this weather event. Hence, numerical simulations of this case study are also performed with the OpenIFS model.

b. OpenIFS

ECMWF maintains and develops the Integrated Forecast System (IFS), which includes a data assimilation system, forecast systems for the atmosphere and ocean, as well as a wave and sea ice model. The IFS is a global, hydrostatic spectral model that uses semi-implicit semi-Lagrangian time stepping that enables long time steps while remaining numerically stable (Staniforth and Côté 1991; Ritchie et al. 1995; Temperton et al. 2001; Hortal 2002). Parameterizations for radiation, microphysics, turbulence, convection, gravity wave drag, and surface fluxes are included. The full IFS documentation is available online (ECMWF 2019). The IFS is used operationally to produce weather forecasts as well as extended-range and seasonal predictions. In addition, the IFS is also the forecast system used to produce the ERA-Interim reanalysis (Dee et al. 2011).

OpenIFS is a version of the IFS that is available to academic and research institutions free of charge but under license for use in research and teaching (Szépszó and Carver 2018; Szépszó et al. 2019). OpenIFS has exactly the same dynamics and physical parameterizations as the atmospheric model of the full version of the IFS and also includes the same wave model. However, OpenIFS does not contain the data assimilation system, sea ice model nor ocean model. OpenIFS version Cy40r1v1 is used in this study to perform numerical simulations of Hurricane Debby and its evolution into extratropical storm Mauri. The equivalent version of the IFS was operational between November 2013 and May 2015. All simulations included here are global simulations initialized from ERA-Interim reanalysis data and are run with a horizontal spatial resolution of approximately 16 km (T1279 in spectral space) and with 137 vertical levels. Coarser-resolution simulations, when compared to ERA-Interim reanalysis data, were found to not correctly capture the complete evolution of Hurricane Debby/extratropical storm Mauri (not shown). The simulations were run with a 10-min time step and model fields were output every hour.

c. 10-m wind speed and gust parameterization

The OpenIFS simulations are used to assess the physical mechanisms that resulted in the strong winds over northern Finland. Therefore, a brief overview of how the full IFS and thus OpenIFS parameterizes the 10-m wind speed and the 10-m wind gust is given here.

A full description is available in the IFS documentation (ECMWF 2015).

The method used to compute the 10-m wind in the operational IFS and thus OpenIFS is designed so that the resulting wind speeds are as comparable as possible to 10-m wind speeds measured at SYNOP stations. Official SYNOP stations are located in open terrain and are well exposed to the wind. Therefore, standard SYNOP observations of 10-m wind are not necessarily representative of a larger area, for example, the area of a grid box in a model. A model grid box is likely to be inhomogeneous and include rougher elements, for example forest, which results in a higher aerodynamics roughness value than for open homogeneous terrain. To account for this, an exposure correction is applied online during the model run (i.e., it is part of the OpenIFS model code) to grid boxes where the roughness length exceeds 0.03 m. This uses wind values at a level (40 m above ground level) that are not strongly affected by the surface and interpolates these to 10 m using an aerodynamic roughness length, which is representative of open terrain with grassland and thus comparable to the terrain at SYNOP stations. Therefore, it should be noted that 10-m wind speeds output from OpenIFS may be higher than reality at some locations but that overall they should compare well with observations.

Wind gusts are also computed by the OpenIFS code and the method employed is designed to ensure the model output is directly comparable to how wind gusts are observed following the World Meteorological Organization's recommendations. In OpenIFS, the wind gust (F_{gust}) is calculated as:

$$F_{gust} = F_{10} + C_{ugn} u_* + C_{conv} \max(0, U_{850} - U_{950}) \quad (1)$$

where F_{10} is the 10-m wind speed calculated as described above, C_{ugn} is an empirically derived parameter and has a value of 7.71, u_* is the friction velocity, C_{conv} is the convective mixing parameter and has a value of 0.6, and U_{850} and U_{950} are the wind speeds at 850 and 950 hPa, respectively (ECMWF 2015). The second term on the right-hand side represents turbulent driven wind gusts and thus includes the effects of surface friction (through surface roughness) and boundary layer stability. The third term represents wind gusts generated by the downward transport of higher momentum air that can occur in convective situations (Bechtold and Bidlot 2009), which may be organized downdrafts in a sheared environment or evaporatively driven downdrafts. This convective term only becomes active during time steps and at grid points where the horizontal wind speed increases with height and where the convection scheme is active. In practice, this term contributes to forecast wind gusts in frontal systems and in organized mesoscale convective systems.

The wind gust (F_{gust}) is computed every time step during the simulation and its maximum value since the last postprocessing is written to the output files. Here we output model variables every hour so the wind gusts we obtain are the maximum gust to have occurred in the previous hour. We do not directly output the turbulent or convective wind gust terms [second and third terms on the right-hand side of Eq. (1)]. Instead, these two terms are approximated offline from the hourly outputs of the instantaneous eastward and northward turbulent surface stress components and wind speeds at 850 and 950 hPa. Since the third term is active only during deep convection, we include only grid points where convective precipitation exceeds 1 mm per hour for this term.

d. Observations and additional datasets

IBTrACS (the International Best Track Archive for Climate Stewardship) best track dataset (Knapp et al. 2010) is used to identify the location of Hurricane Debby during the tropical phase and extratropical transition. The data includes longitude and latitude coordinates of the cyclone, the minimum sea level pressure and the 1-min averaged sustained surface wind speeds.

We also investigated SYNOP observations from Finnish Meteorological Institute (FMI) from the time the storm was over Finland (22 September 1982). We obtained 10-m wind speed observations in total from 130 automated and manual weather stations. In 1982, when storm Mauri occurred, wind speed observations were made as 10-min average SYNOP observations every 3 h or every 6 h. Therefore, taking into account the temporal (and spatial) resolution, the highest wind speeds associated with storm Mauri are likely to be missing from FMI's observational dataset. No wind gust observations were made at that time.

Additionally, we obtained several thermal infrared satellite images from the Advanced Very High Resolution Radiometer (AVHRR) from the NERC Satellite Receiving Station, Dundee University, Scotland.

3. Analysis methods

a. Cyclone space phase diagram

Hart (2003) developed an objective methodology that can be used to visually detect the evolution of the ET process through a phase diagram. A phase diagram has $-V_T^L$ values on the x axis and B values on the y axis, which represent the thermal wind and storm symmetry, respectively. ET onset is defined to occur when the storm symmetry parameter B becomes greater than

10 m denoting that the cyclone changes from symmetric to asymmetric. Tropical cyclones are warm cored and thus, the geostrophic wind decreases with height (negative thermal wind) whereas extratropical cyclones are cold cored and the geostrophic wind increases with height (positive thermal wind). Therefore, ET completion is defined to occur when $-V_T^L$ becomes negative denoting that the cyclone changes to cold cored.

b. Quasigeostrophic omega equation

The quasigeostrophic omega equation is a diagnostic equation which can be solved for the vertical velocity. The traditional form of the omega equation partitions the forcing for vertical motion into a thermal advection term and a differential vorticity advection term (Holton and Hakim 2013), which due to the linearity of the equation can be solved separately. Warm-air advection and vorticity advection increasing with height are forcings for ascent, whereas cold-air advection and vorticity advection decreasing with height are forcings for descent.

Here we solve the following version of the omega equation that is formulated in pressure coordinates:

$$\sigma_0(p)\nabla^2\omega + f^2\frac{\partial^2\omega}{\partial p^2} = f\frac{\partial}{\partial p}[\mathbf{V}\cdot\nabla(\zeta+\mathbf{f})] + \frac{R}{p}\nabla^2(\mathbf{V}\cdot\nabla T),$$
(2)

where σ_0 is the hydrostatic static stability, taken here to be the average on each pressure surface, p is pressure, ω is the vertical velocity in pressure coordinates (units $\mathrm{Pa\,s}^{-1}$), f is the Coriolis parameter, $\mathbf{V}$ is the horizontal wind vector, ζ is the relative vorticity and T is temperature. In this formulation the full winds and relative vorticity are used, rather than the geostrophic values typically applied in the traditional formulation as this increases the agreement between the diagnosed omega and the model output omega. The vertical motion diagnosed with Eq. (2) was compared to the model output omega values (Fig. S1 in the online supplemental material) and in general a good agreement was found particularly on synoptic scales. Furthermore, in this version of the omega equation the contribution of friction and diabatic heating have been neglected.

OpenIFS model output on evenly spaced pressure surfaces every 50 hPa at the native model resolution (T1279) is used as input to Eq. (2). The terms on the right-hand side are first calculated in grid-point space and then the equation is solved in spectral space. Due to the high resolution, the resultant omega fields are rather noisy when calculated at T1279 resolution. Therefore, a smoothing is applied when solving the omega equation such that the Fourier coefficient

associated with wavenumbers larger than T255 are set to zero. This effectively smooths the output from the omega equation to T255 resolution, approximately 80 km.

Sutcliffe's development theorem (Sutcliffe 1947) links vertical motions to surface development via the quasigeostrophic vorticity equation:

$$\frac{\partial\zeta_g}{\partial t} = -\mathbf{V}_g\cdot\nabla(\zeta_g+f) + f_0\frac{\partial\omega}{\partial p}.$$
(3)

Assuming the standard boundary condition that $\omega = 0$ at the surface, Eq. (3) shows that if there is ascent in the low-to-mid troposphere, $\partial\omega/\partial p > 0$, and thus this will cause an increase in low-level relative vorticity. Ascent therefore leads to the intensification of a surface cyclone, and therefore when vertical motions due to different forcings are diagnosed from the omega equation, we can subsequently infer how the surface cyclone will develop.

4. Synoptic overview

In this section, we provide a brief synoptic overview of Debby and other relevant synoptic-scale features in the North Atlantic based on ERA-Interim reanalysis. An animation of the 850-hPa relative vorticity with 6-hourly time steps is included in the supplemental material to show that a coherent low-level positive vorticity anomaly can be tracked from Hurricane Debby across the Atlantic and finally to northern Finland. Four distinct stages of the evolution of the hurricane and the extratropical windstorm are considered here: 1) Hurricane Debby, 2) extratropical transition, 3) reintensification over the United Kingdom, and 4) storm Mauri in northern Finland.

a. Hurricane Debby

Debby was a category 4 hurricane, with maximum sustained winds of $58\,\mathrm{m\,s}^{-1}$, that formed from a tropical depression north of the Dominican Republic on 13 September 1982 (Clark 1983). It developed into a tropical storm at 1200 UTC 14 September and was upgraded to a hurricane 12 h later at 0000 UTC 15 September while moving north from the Bahamas (Clark 1983). Between 15 and 17 September, Debby took a more northeastward course both in the IBTrACS best track data and minimum central pressure track of ERA-Interim, which we produced manually by following the minimum mean sea level pressure center associated with Debby (Fig. 1a). The hurricane deepened rapidly, which was captured only in IBTrACS (Fig. 1b); reanalysis datasets, like ERA-Interim, are
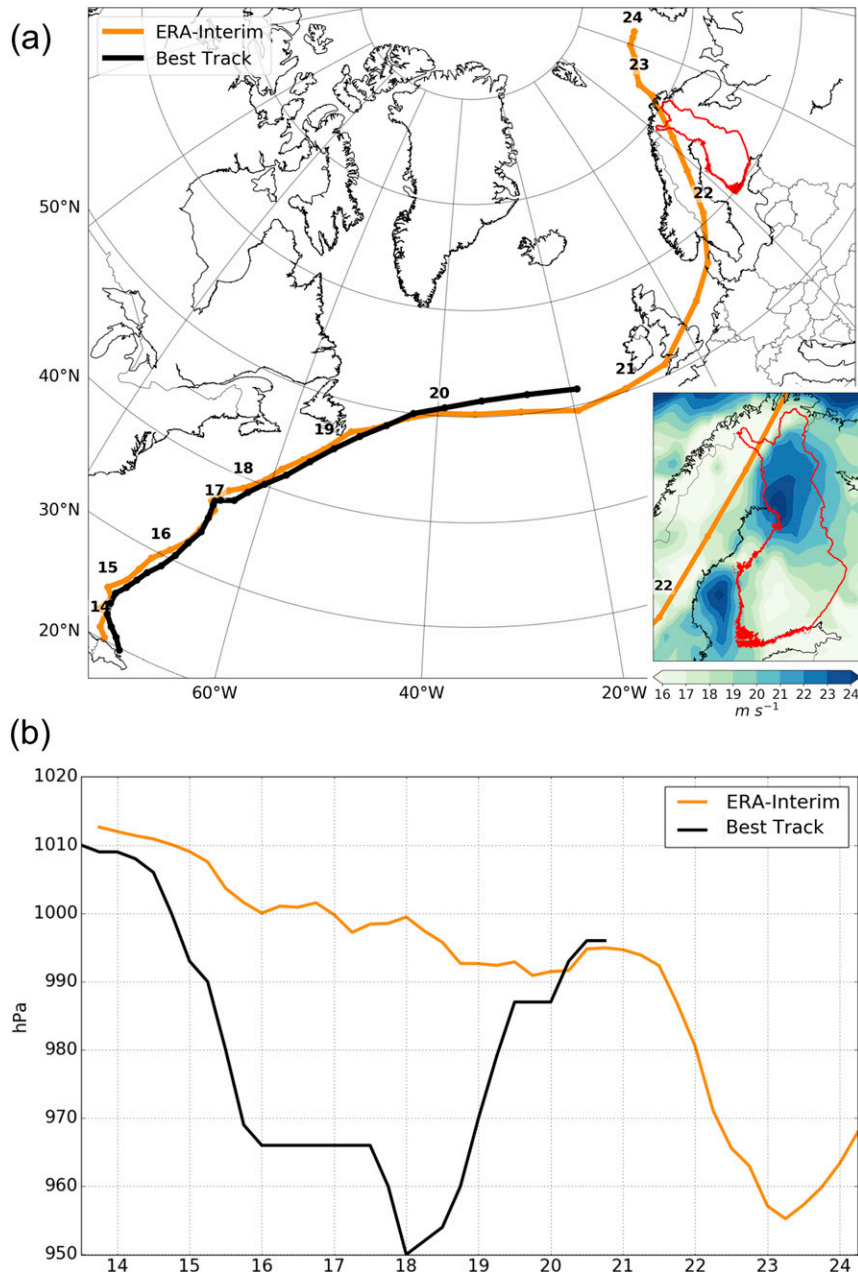
FIG. 1. (a) IBTrACS best track for Hurricane Debby (black) and ERA-Interim manual minimum sea level pressure track (orange). Dots are plotted every 6 h and the labeled numbers are days of September 1982 at 0000 UTC. The inset figure shows maximum 10-m wind gusts between 21 and 24 Sep 1982 from ERA-Interim (colors, m s^{-1}). Borders of Finland are colored red. (b) Time series of minimum mean sea level pressure for Hurricane Debby from IBTrACS best track (black) and ERA-Interim (orange).

known to often underestimate hurricane intensity (Schenkel and Hart 2012; Hodges et al. 2017). The phase diagram, created based on ERA-Interim data, shows that Debby had a warm core ($-V_T^L > 0$) and symmetric structure ($B < 10$ m) as typical for a tropical system (Fig. 2).

At 1200 UTC 16 September, Debby was located at 32°N, 65°W and the symmetrical vortex of the hurricane was visible in the 850-hPa relative vorticity and mean sea level pressure (MSLP) fields (Fig. 3a). At that time, there was a small, additional 850-hPa relative vorticity maximum evident at 47°N, 73°W that was in the
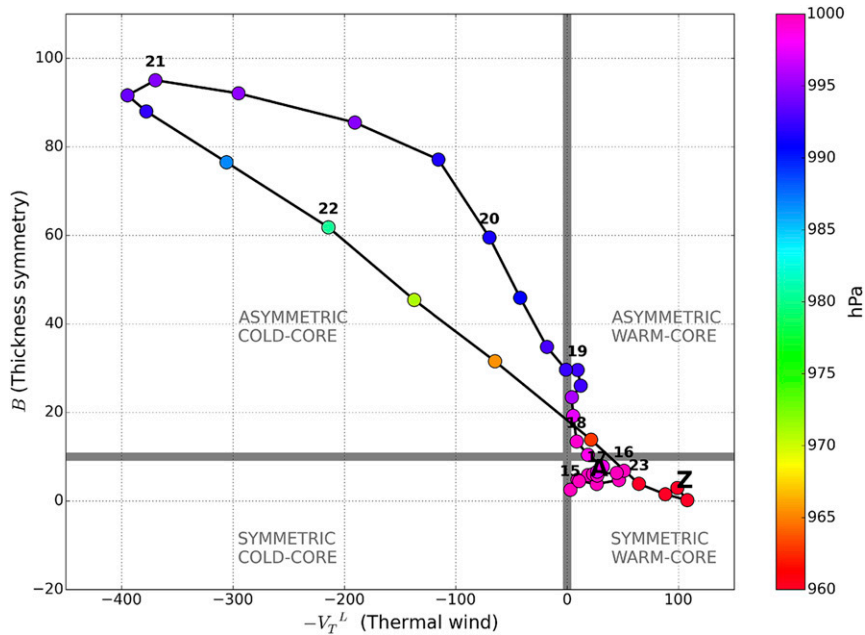
FIG. 2. Phase diagram of Hurricane Debby based on ERA-Interim. Dots are plotted every 6 h and the labeled numbers above the dots are days of September 1982 at 0000 UTC (starting with letter "A" at 1200 UTC 14 Sep and ending with letter "Z" at 1800 UTC 23 Sep). The dot colors indicate mean sea level pressure of the cyclone.

left-hand exit region of a jet streak, an ideal location for further development. Debby potentially enhanced the development of this feature by advecting warm and moist air poleward, although the favorable location relative to the jet streak likely contributed to the cyclone development. The jet streak over North America reached wind speeds of $50 \, \mathrm{m \, s^{-1}}$ at 300 hPa and another jet streak with wind speeds exceeding $60 \, \mathrm{m \, s^{-1}}$ at 300 hPa extended from the central North Atlantic to northern Europe. Twelve hours later, at 0000 UTC 17 September, Debby moved northward and a surface low (hereinafter referred to as "ETC1") became evident north of Debby at 50°N, 72°W (Fig. 3b). ETC1 traveled east and at 1200 UTC 17 September it had reached Newfoundland (Fig. 3c).

b. Extratropical transition

Based on the phase diagram, ET onset occurred at 1800 UTC 17 September as Debby became asymmetric i.e., the B value exceeded 10 m (Fig. 2). Debby reached a minimum surface pressure of 950 hPa at 0000 UTC 18 September (Fig. 1b) while located at 37°N, 62°W (Figs. 1a and 3d). The 850-hPa relative vorticity maximum related to ETC1 had increased and spatially extended, while another closed low center formed between Greenland and Iceland at 65°N, 35°W with a minimum MSLP of 1000 hPa (hereinafter referred to as "ETC2"). At 1200 UTC 18 September, Debby still had a rather

symmetrical vortex noted from the 850-hPa relative vorticity and MSLP patterns (Fig. 4a). ETC1 traveled east over the Atlantic while ETC2 remained stationary. There was a jet streak that had wind speeds exceeding $60 \, \mathrm{m \, s^{-1}}$ at 300 hPa over northern Europe and a weaker jet of $40 \, \mathrm{m \, s^{-1}}$ at 300 hPa over the northeastern Atlantic.

Debby moved slowly toward the north and east, and by 0000 UTC 19 September it had reached Newfoundland (Figs. 1a and 4b). At 0600 UTC 19 September, the phase diagram shows Debby becoming cold cored ($-V_T^L$ turning negative) indicating the ET completion and a transformation of Hurricane Debby to an extratropical cyclone, now referred to as "ex-Debby" (Fig. 2). The shape of MSLP and 850-hPa relative vorticity near the center of the storm started to spread zonally (Figs. 4c,d). ETC2 moved east toward Iceland and at 1200 UTC 19 September it had intensified with the minimum MSLP of 996 hPa while ETC1, also deepening to a minimum of 998 hPa, rapidly traveled eastward across the Atlantic (Fig. 4c). ETC1 was located at the left exit of the intensifying jet, now exceeding $60 \, \mathrm{m \, s^{-1}}$ at 300 hPa.

At 1200 UTC 19 September, ex-Debby came under the influence of the midlatitude westerlies and moved rapidly across the Atlantic; between 1200 UTC 19 September (Fig. 4c) and 0000 UTC 21 September (Fig. 4f) ex-Debby traveled almost 2700 km in 36 h.
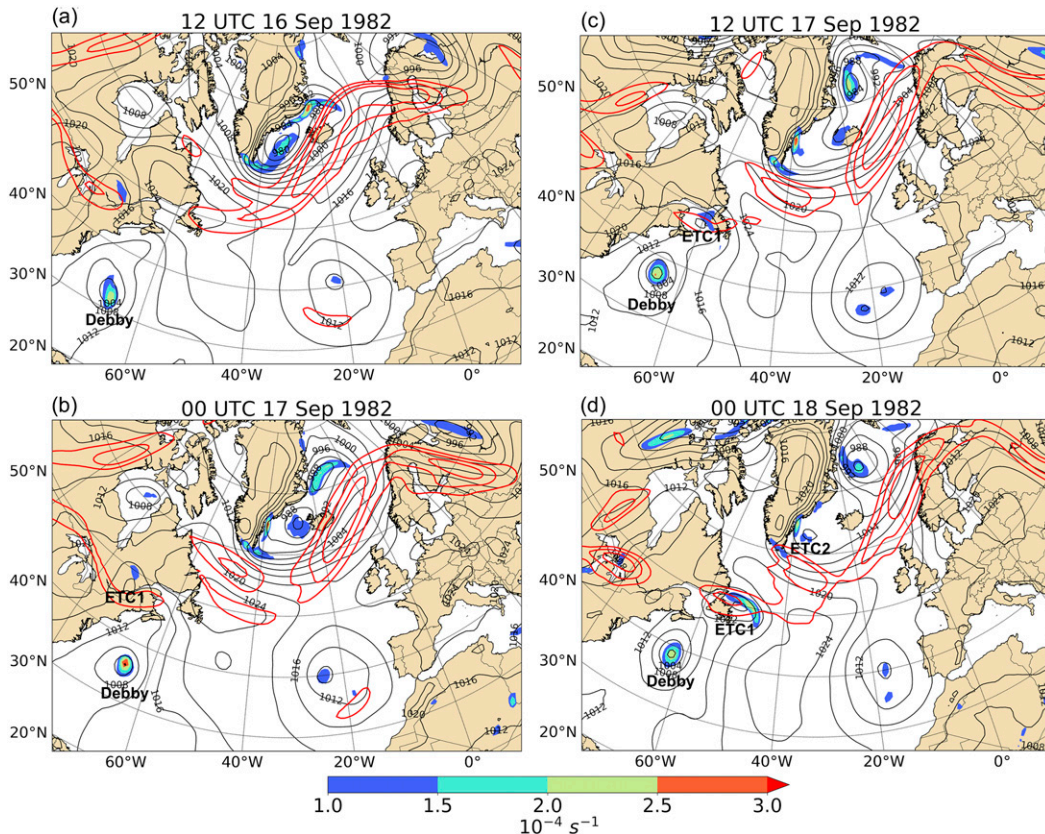
FIG. 3. 850-hPa relative vorticity (colors, s^{-1}), 300-hPa wind speed (red contours at 40, 50, and $60\,m\,s^{-1}$), and mean sea level pressure (black contours at 4-hPa interval) from ERA-Interim at (a) 1200 UTC 16 Sep, (b) 0000 UTC 17 Sep, (c) 1200 UTC 17 Sep, and (d) 0000 UTC 18 Sep.

By 1200 UTC 20 September, when located at 50°N, 25°W (Fig. 4e), ex-Debby had a much larger zonal than meridional extent, values of 850-hPa relative vorticity reaching $3 \times 10^{-4}\,s^{-1}$ and a minimum MSLP of 994 hPa. Farther east and north of ex-Debby, between Iceland and the United Kingdom, ETC1 merged with ETC2, leading to the development of a large intense low pressure system with 984-hPa minimum pressure.

c. Reintensification over the United Kingdom

At 0000 UTC 21 September, the 850-hPa positive vorticity anomaly associated with ex-Debby had a coherent structure (Fig. 4f) but 12 h later, the vorticity anomaly magnitude had decreased (Fig. 5a). Between those 12 h, 0000–1200 UTC 21 September, ex-Debby traveled from southwestern Ireland (50°N, 10°W, Fig. 4f) across the southern United Kingdom to the North Sea (55°N, 5°E, Fig. 5a). The MSLP pattern resembled a frontal trough rather than a closed low (Figs. 4f and 5a), which is also detected in the satellite image valid at 0422 UTC 21 September (Fig. 6); there was a frontal wave visible over the central

United Kingdom alongside the cold front of the mature extratropical cyclone.

To the north of ex-Debby, the large low pressure system (merged ETC1 and ETC2) continued to intensify over the Norwegian Sea reaching a minimum MSLP of 968 hPa (Fig. 5a). The 850-hPa relative vorticity indicated a strong bent-back warm front to the north and east of the low pressure center and a cold front to the south. Such a frontal structure resembles the T-bone structure of the Shapiro–Keyser cyclone model (Shapiro and Keyser 1990). The occurrence of the mature extratropical cyclone is confirmed from the satellite image (Fig. 6) with a pronounced hook cloud and dry intrusion wrapping around the center of the cyclone.

At 1200 UTC 21 September, ex-Debby was situated beneath the right-hand side of jet entrance region, which likewise the left-hand side exit region is a favorable area for further cyclone development (Fig. 5a). At that time, the asymmetric and cold core structure of ex-Debby started to change as the high B values began to decrease and highly negative $-V_T^L$ values began to increase toward zero (Fig. 2). The surface pressure of ex-Debby
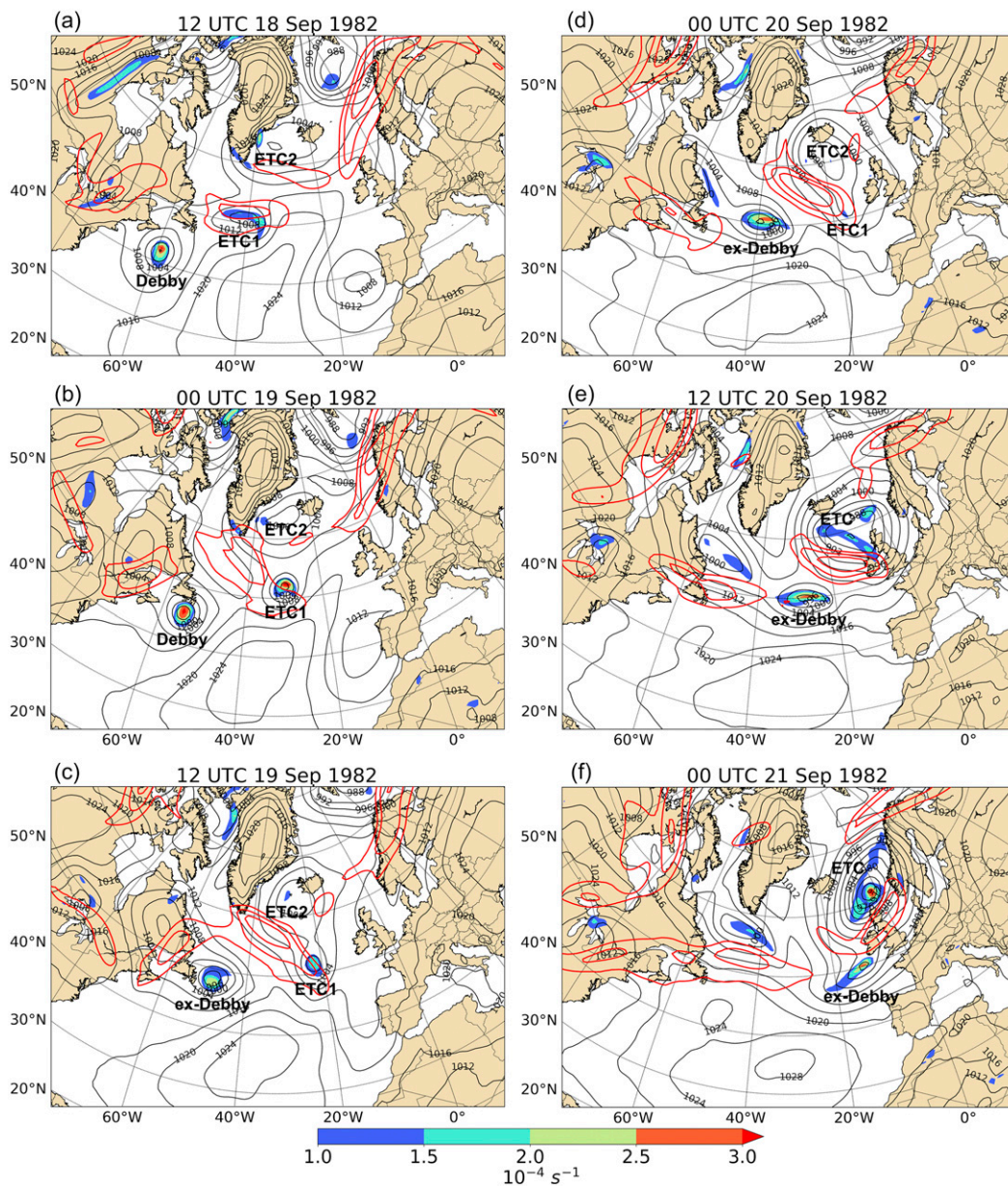
FIG. 4. 850-hPa relative vorticity (colors, s^{-1}), 300-hPa wind speed (red contours at 40, 50, and 60 m s^{-1}), and mean sea level pressure (black contours at 4-hPa interval) from ERA-Interim at (a) 1200 UTC 18 Sep, (b) 0000 UTC 19 Sep, (c) 1200 UTC 19 Sep, (d) 0000 UTC 20 Sep, (e) 1200 UTC 20 Sep, and (f) 0000 UTC 21 Sep.

started to rapidly deepen (Fig. 1b) and 12 h later, at 0000 UTC 22 September, the 850-hPa positive vorticity anomaly of ex-Debby had reintensified (Fig. 5b).

d. Storm Mauri in northern Finland

At 0000 UTC 22 September, there were two closed low pressure centers evident and three separate localized 850-hPa relative vorticity maxima (Fig. 5b). The relative vorticity maximum associated with ex-Debby was in southern Sweden at 61°N, 15°E and did

not have a closed low pressure contour. The second relative vorticity maximum was located over the Norwegian Sea, related to the occlusion, and had a 972 hPa minimum pressure. The third relative vorticity maximum was north of 70°N, had a minimum MSLP of 976 hPa, and was related to the warm front extending toward the east in the Barents Sea. Twelve hours later at 1200 UTC, the low pressure center and vorticity maximum associated with ex-Debby had strengthened and moved northward (Fig. 5c). Two other vorticity
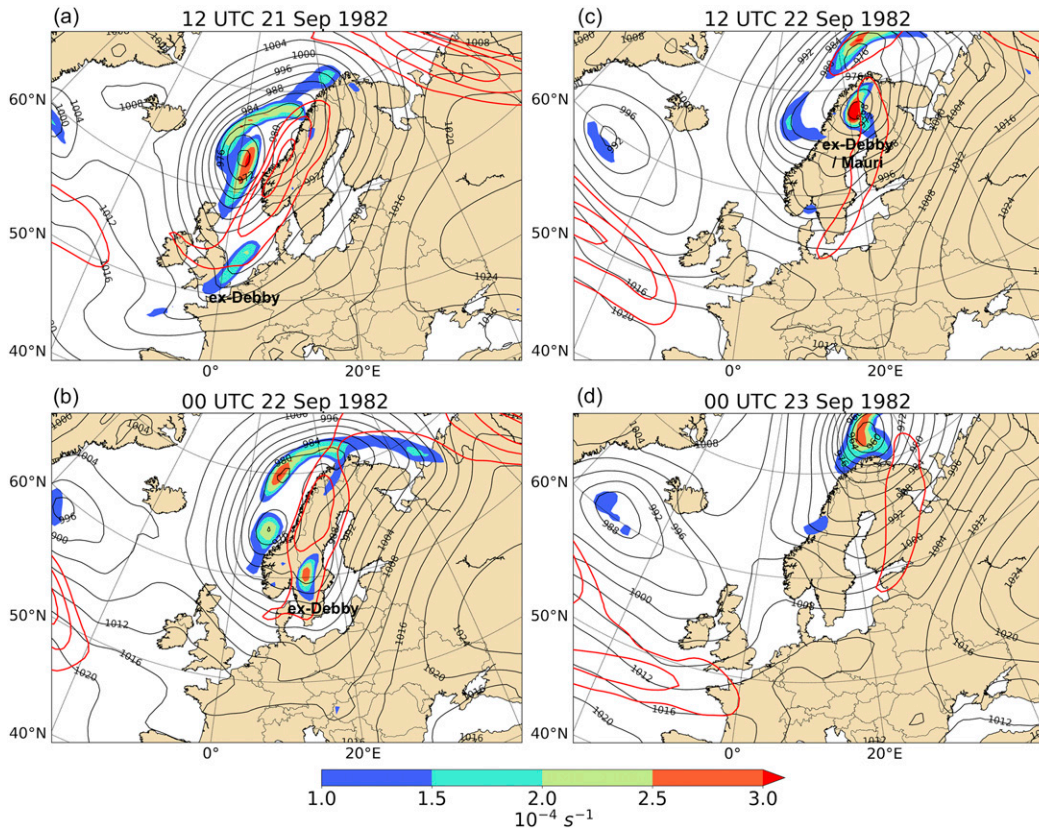
FIG. 5. 850-hPa relative vorticity (colors, s^{-1}), 300-hPa wind speed (red contours at 40, 50, and 60 m s^{-1}), and mean sea level pressure (black contours at 4-hPa interval) from ERA-Interim at (a) 1200 UTC 21 Sep, (b) 0000 UTC 22 Sep, (c) 1200 UTC 22 Sep, and (d) 0000 UTC 23 Sep.

centers, one in the Norwegian Sea and one in the Barents Sea, remained at this time but only the Barents Sea vorticity maximum was associated with a closed pressure contour (Fig. 5c). The low related to the remains of the warm front had moved farther north. The low center associated with ex-Debby, now located in northern Sweden at 68°N, 21°E, was clearly the more intense of the two with minimum pressure of 965 hPa. The region of 850-hPa relative vorticity maximum was widely spread and exceeded $3 \times 10^{-4} \, \mathrm{s}^{-1}$. This strong low center moved over northern Finland and was named storm Mauri. The maximum 10-m wind gusts attained in ERA-Interim during storm Mauri were up to 26 m s^{-1} and there was a large area over Finland where the gusts exceeded 20 m s^{-1} (enlarged box in Fig. 1a). The phase diagram shows that ex-Debby/storm Mauri became warm cored at 1800 UTC 22 September and regained symmetric structure at 0000 UTC 23 September (Fig. 2). This change in the structure was due to the warm air seclusion, a feature typically observed in fully developed T-bone structure cyclones, which trapped the warm air in the center of the cyclone. The occluded phase of storm Mauri is evident in

Figs. 5c and 5d and in the animation included in the supplemental material.

5. Meso- and synoptic-scale dynamic evolution

a. Overview and verification of OpenIFS simulations

We used OpenIFS to simulate the meso- and synoptic-scale dynamic evolution of ex-Debby and storm Mauri. Three simulations with different initialization dates were conducted. The first simulation was initialized at 0000 UTC 17 September and produces a cyclone track of Hurricane Debby that is in reasonable agreement with ERA-Interim for the first two days (Fig. 7). During those 48 h OpenIFS simulated Debby, still as a hurricane, to move northeast roughly parallel to the east coast of North America. After two days of simulation, errors develop in the OpenIFS forecast initialized on 17 September and ex-Debby is simulated to track farther south than in ERA-Interim. During 19 and 20 September, the minimum MSLP simulated is 3–15 hPa higher than in ERA-Interim. Therefore, the forecast from 17 September is only used to investigate how Debby modified the midlatitude flow in section 5b.
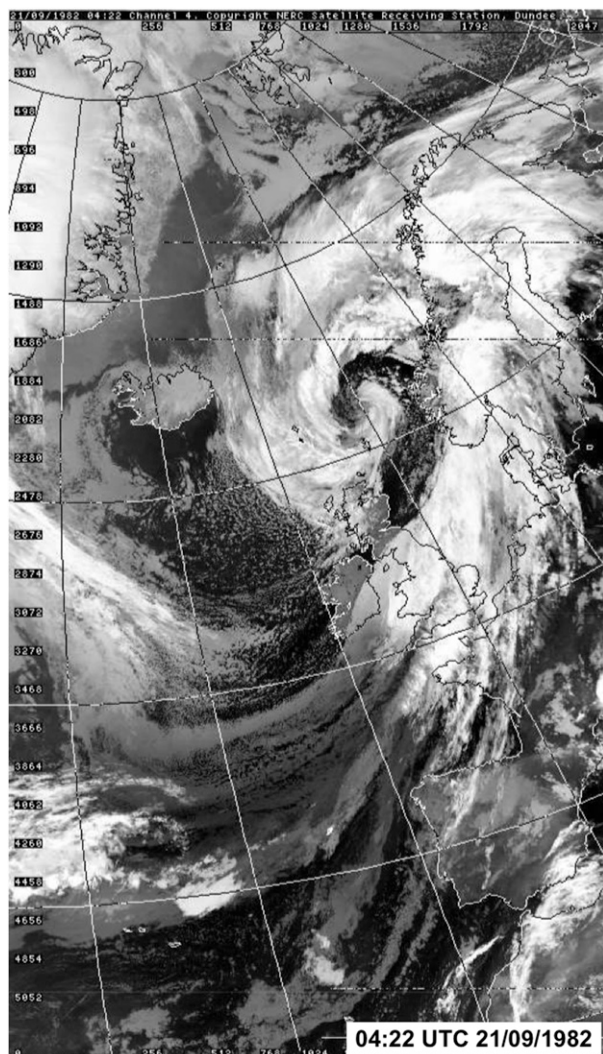
FIG. 6. Thermal infrared satellite image obtained from the Advanced Very High Resolution Radiometer (AVHRR) at 0422 UTC 21 Sep 1982. Copyright NERC Satellite Receiving Station, Dundee University, Scotland.

The second simulation was initialized at 0000 UTC 19 September; the track of ex-Debby in this OpenIFS forecast compares well against ERA-Interim for two days (19 and 20 September) during which time the cyclone traveled from Newfoundland across the Atlantic to the south of Ireland (Fig. 7). However, on 21 September when ex-Debby traveled over the south of the United Kingdom and reintensified, large differences appear between the OpenIFS forecast and ERA-Interim. The OpenIFS simulated track of ex-Debby is farther south than in ERA-Interim and the simulated minimum MSLP increases during 21 September demonstrating that the OpenIFS forecast initialized on 19 September cannot correctly capture the reintensification that took place over the United Kingdom. Hence, the forecast from

19 September is only used to analyze the large-scale flow and dynamical evolution and structure of ex-Debby as it traveled across the Atlantic in section 5c.

The third simulation was initialized at 0000 UTC 21 September. Both the simulated track location and intensity agree well with ERA-Interim during 21 and 22 September (Fig. 7). Therefore, the forecast from 21 September is used to investigate the reintensification of ex-Debby over the United Kingdom (section 5d) and the high winds over Finland (section 5e). Since in the OpenIFS forecast initialized on 19 September ex-Debby decayed and did not reintensify over the United Kingdom, we compared that to the forecast initialized on 21 September to attempt to identify the reasons for the redevelopment. In addition, as there was no ex-Debby over northern Finland in the forecast initialized on 19 September, we qualitatively estimate the role that ex-Debby played in leading to the strong winds and to the occurrence of storm Mauri by comparing the winds simulated in the forecast initialized on 19 September to those in the forecast initialized on 21 September (section 5f).

b. Did Debby modulate the downstream upper-level flow?

Debby did not begin the process of ET until 1800 UTC 17 September but had already started to impact the evolution of the midlatitude flow before this time. As noted in section 4a, Debby may have affected the midlatitude flow on 16 September by enhancing the development of ETC1. Later on Debby started to directly impact the midlatitude flow. At 0600 UTC 18 September, 12 h after the transition process began, Debby was located at 41°N, 60°W (Figs. 7a and 8a). The upper-level waveguide, indicated by the 2 potential vorticity unit (2 PVU) contour (1 PVU = $1.0 \times 10^{-6}\,\mathrm{m^2\,s^{-1}\,K\,kg^{-1}}$) in Fig. 8a, was already somewhat amplified at this time. A trough, visible in the 200-hPa PV, was located upstream of Debby, a pronounced ridge was present to the north and downstream of Debby and ETC1 was at 51°N, 50°W collocated with a 200-hPa jet streak that had a maximum speed of 69 m s^{-1} (Fig. 8a). In addition, at 0600 UTC 18 September strong divergent (irrotational) winds at 200 hPa were associated with Debby. Directly above and slightly west of Debby's center, upper-level divergent winds, which were likely a result of the outflow from Hurricane Debby, were directed toward the west that may have impeded the eastward progression of the upstream trough. Strong divergent winds were also present to the north of Debby, over Newfoundland, and were almost perpendicular to the PV gradient at 200 hPa. The divergent winds were directed from a region of low-PV air at 200 hPa, which most likely arose due to diabatic heating in the low-to-mid troposphere, to an area of high
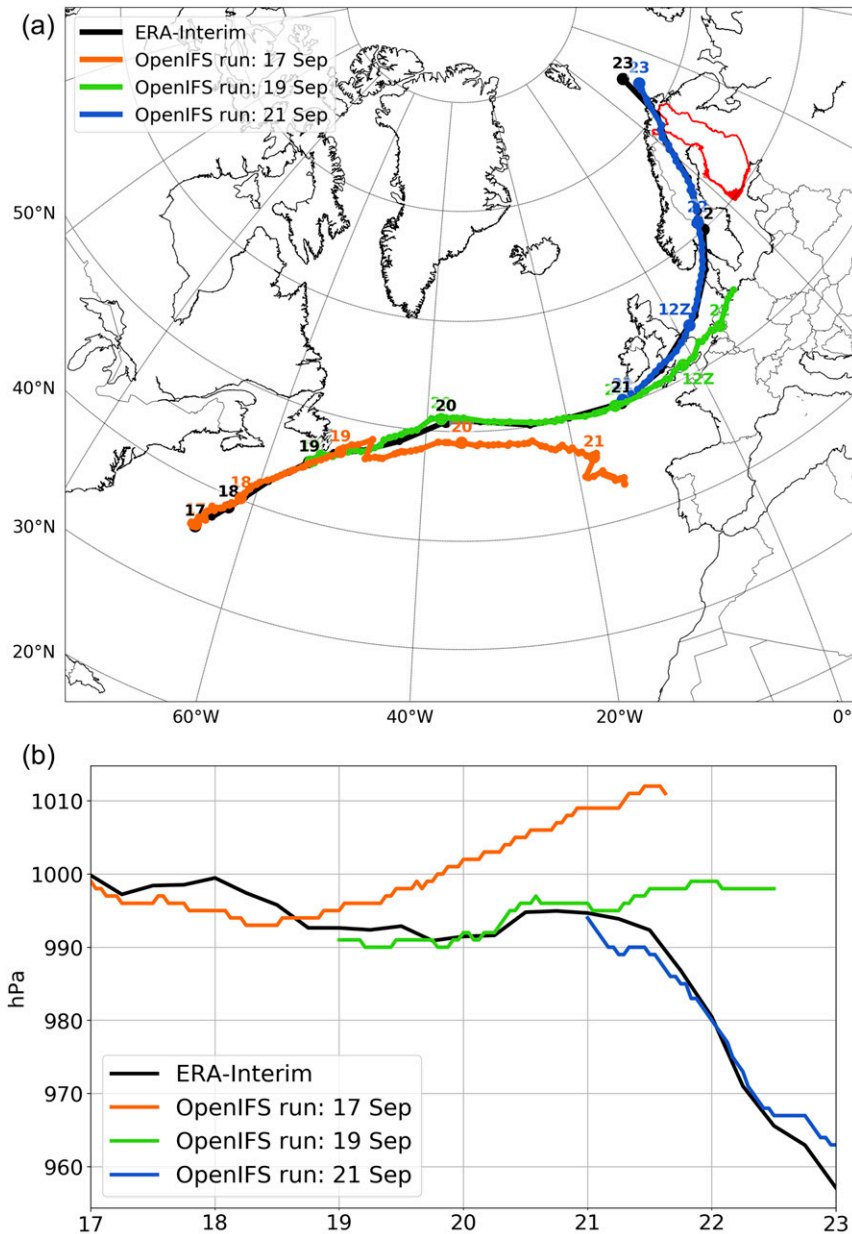
FIG. 7. (a) Manual 850-hPa maximum vorticity tracks from ERA-Interim (black) and OpenIFS simulations initialized on 17 Sep (orange), 19 Sep (green), and 21 Sep (blue). Dots are plotted every 6 h for ERA-Interim and every hour for the OpenIFS forecasts. The labeled numbers above the enlarged dots are days of September 1982 at 0000 UTC, in addition 1200 UTC 21 Sep is labeled. Borders of Finland are colored red. (b) Time series of minimum mean sea level pressure for ERA-Interim (black) and OpenIFS simulations initialized on 17 Sep (orange), 19 Sep (green), and 21 Sep (blue).

PV. Therefore, the upper-level divergent winds resulted in negative PV advection at upper levels.

At 1800 UTC 18 September, strong 200-hPa divergent winds remained collocated with the PV gradient, and the upper-level ridge to the north of Debby had amplified slightly (Fig. 8b). Furthermore, at 1800 UTC

18 September the jet streak had strengthened slightly and now had a maximum speed of 76 m s^{-1}. The jet likely accelerated due to the influx of low-PV air on the equatorward side of the jet, which would act to steepen the tropopause and consequently accelerate the jet stream. This sequence of events, namely weak ridge
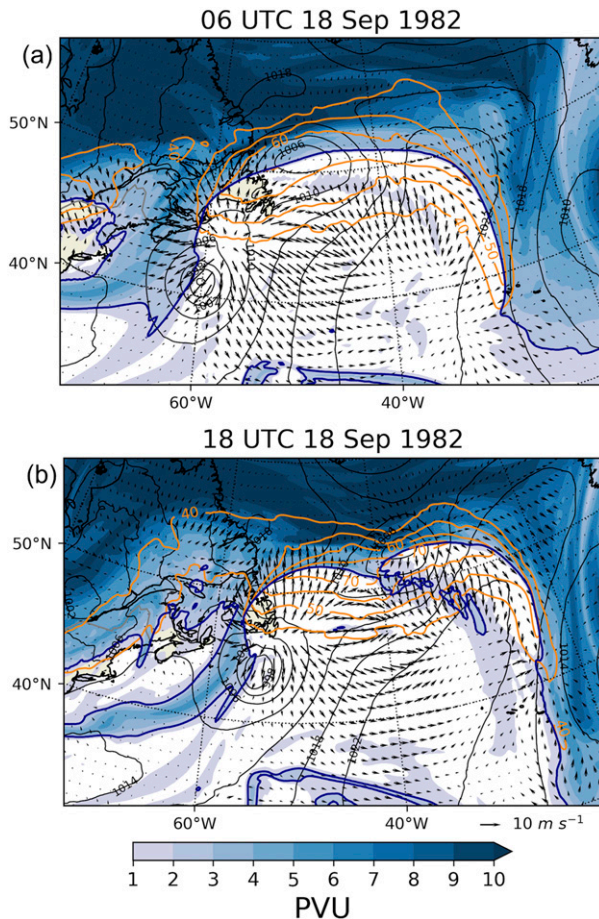
06 UTC 18 Sep 1982

FIG. 8. OpenIFS simulation initialized on 17 Sep valid at (a) 0600 UTC 18 Sep, and (b) 1800 UTC 18 Sep. 200-hPa potential vorticity (colors, 2 PVU contour also in dark blue), 200-hPa divergent wind (vectors), 200-hPa wind speed (orange contours starting at $40\,\mathrm{m\,s^{-1}}$ with $10\,\mathrm{m\,s^{-1}}$ interval), and mean sea level pressure (black contours at 4-hPa interval).

building and jet streak acceleration, is similar to that observed during the transition of Typhoon Jangmi in 2008 (Grams et al. 2013). It is notable that the minimum MSLP of Debby did not decrease between 0600 and 1800 UTC 18 September despite the presence of an upper-level trough immediately to the west. Previous studies (e.g., Riboldi et al. 2019) have shown that reintensification of tropical cyclones can be very sensitive to the exact location and propagation speed of the trough axis. Thus, a small shift in the position of Debby, or the upper-level trough, could have easily resulted in a very different evolution of ex-Debby.

c. Why was ex-Debby able to travel across the North Atlantic?

Ex-Debby moved rapidly across the North Atlantic between 19 and 21 September 1982 in ERA-Interim and

in the OpenIFS forecast initialized on 19 September (Fig. 7a) but did not intensify during this time (Fig. 7b). At 0000 UTC 19 September, Debby was located east of Newfoundland but during the next 48 h ex-Debby traveled almost 3200 km and by 0000 UTC 21 September was located south of Ireland. In this section, we address the cause of this rapid propagation and the cause for the lack of any intensification.

Ex-Debby had completed ET by 0600 UTC 19 September and was located at 46.5°N, 52.5°W, just east of Newfoundland (Fig. 9a). At this time, ex-Debby was positioned under a large-scale upper-level ridge with a trough to the west and another trough to the northeast. The trough to the west, which was associated with potential temperature values of ~300 K on the dynamic tropopause (Fig. 9a), was too far west relative to ex-Debby to provide notable upper-level forcing (this point is further discussed below). This explains the lack of intensification of ex-Debby at this point in time. The second trough, which was located to the east of Greenland at 0600 UTC 19 September, was also at this time unable to interact directly with ex-Debby. This second trough was intense, had closed contours of low (<290 K) potential temperature on the dynamic tropopause at its base (60.8°N, 39°W, Fig. 9a), and was collocated with a surface low pressure center (ETC2).

Twelve hours later, at 1800 UTC 19 September, ex-Debby had tracked eastward and slightly northward and was now located at 49.5°N, 44.8°W whereas the downstream trough had moved east and south (the base of the trough was now located at 58.0°N, 26.2°W) (Fig. 9b). Consequently, ex-Debby was still located under an upper-level ridge and lacked any interaction with this downstream trough. However, as the upper-level downstream trough approached the jet from the northern side it resulted in a further accelerate the jet: at 0600 UTC the maximum 200-hPa wind speed in this jet core was $64.3\,\mathrm{m\,s^{-1}}$ whereas 12 h later it was $70.1\,\mathrm{m\,s^{-1}}$. This upper-level trough proves critical for the reintensification of ex-Debby over the United Kingdom, discussed below in section 5d.

At 0000 UTC 20 September, ex-Debby was located at 50°N, 40°W (Fig. 10a) and remained under the upper-level ridge (Fig. 10e). The minimum MSLP of ex-Debby had not changed over the preceding 24 h yet the PV anomaly and cyclonic circulation associated with ex-Debby remained (Fig. 10a). One physical reason that explains how a PV anomaly of a transitioned tropical cyclone can remain and subsequently redevelop in a baroclinic zone is a diabatic Rossby wave (DRW, e.g., Moore and Montgomery 2004, 2005). Using the criteria of DRW characteristics developed by Boettcher and
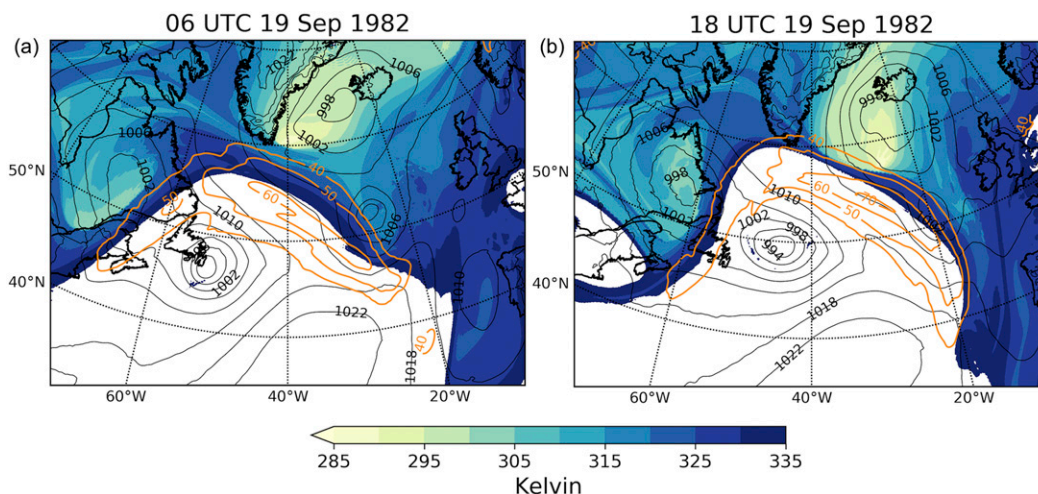
FIG. 9. OpenIFS simulation initialized on 19 Sep valid at (a) 0600 UTC 19 Sep, and (b) 1800 UTC 19 Sep. Potential temperature on the dynamic tropopause (PV = 2 PVU; colors, K), 200-hPa wind speed (orange contours starting at $40\,\mathrm{m\,s^{-1}}$ with $10\,\mathrm{m\,s^{-1}}$ interval), and mean sea level pressure (black contours at 4-hPa interval).

Wernli (2013) (and discussed in section 1), we now test our hypothesis that ex-Debby propagated rapidly across the Atlantic as a DRW.

The first requirement for a DRW is that the MSLP minima is enclosed by a closed MSLP contour. This requirement is clearly met by ex-Debby at both 0000 and 1200 UTC 20 September (Figs. 10a,b). The second requirement is that there must be a positive 850-hPa PV anomaly close to the MSLP minimum. Ex-Debby again meets this criterion as there is a strong positive 850-hPa PV anomaly at both 0000 and 1200 UTC 20 September (Figs. 10a,b), which at 0000 UTC exceeded 5 PVU near the center of the cyclone (Fig. 10a). Vertical cross sections of PV at 0000 UTC 20 September further confirm the presence of a low-level PV anomaly with maximum PV values exceeding 5 PVU between 900 and 700 hPa (Fig. 11). These cross sections also show that ex-Debby still had a vertically coherent PV tower structure remaining from the ET process and consequently the PV anomaly was deeper than typically found in DRWs.

The third requirement is that there must be substantial low-level baroclinicity. At 0000 UTC 20 September, there was a strong horizontal potential temperature gradient (and equivalent potential temperature gradient—not shown) downstream of ex-Debby (Fig. 10c). In the climatological study by Boettcher and Wernli (2013), the specific criteria for low-level baroclinicity is that the difference between the 10th and 90th percentile of 950-hPa potential temperature difference evaluated over a box downstream of the cyclone center must exceed 5 K. This box starts 1.2°E of the MSLP minima and extends a further 3.6°E and extends 1.8°S and 4.8°N of the cyclone center. However, in case studies values

much higher than 5 K can occur. For example, a DRW event from December 2005 had baroclinicity values exceeding 14 K (Boettcher and Wernli 2011). The same method for estimating baroclinicity as used by Boettcher and Wernli (2011) and Boettcher and Wernli (2013) was applied to the OpenIFS output. At 0000 (1200) UTC 20 September a value of 15.5 K (12.3 K) was found that exceeds the threshold and confirms that the requirement of a strong baroclinic zone is also met.

The fourth requirement of Boettcher and Wernli (2013) is that the cyclone must travel more than 250 km within 6 h to meet the requirement of fast propagation. Between 0000 and 0600 UTC 20 September ex-Debby traveled 480 km and between 0600 and 1200 UTC 20 September ex-Debby traveled another 510 km (Fig. 7a). Hence, ex-Debby fulfills the fast propagation speed criterion. Ex-Debby also had sufficient moisture (the fifth requirement); 850-hPa relative humidity around the cyclone center exceeded 90% at both 0000 and 1200 UTC 20 September (Figs. 10c,d). In addition, at both 0000 and 1200 UTC 20 September, diabatic heating due to microphysics and convection averaged over the 900–700-hPa layer exceed $1\,\mathrm{K\,h^{-1}}$ immediately downstream of ex-Debby (Figs. 10e,f). Thus, based on the first five criteria, ex-Debby qualifies as a DRW at both 0000 and 1200 UTC 20 September and certainly at low-level has strong similarities with DRWs.

The final requirement of a DRW is that there is very weak upper-level forcing. Vertical cross sections indicate that there were strong, large-scale troughs (positive PV anomalies descending from the stratosphere) both to the northwest (Fig. 11a) and northeast (Fig. 11b) of ex-Debby but that neither of these
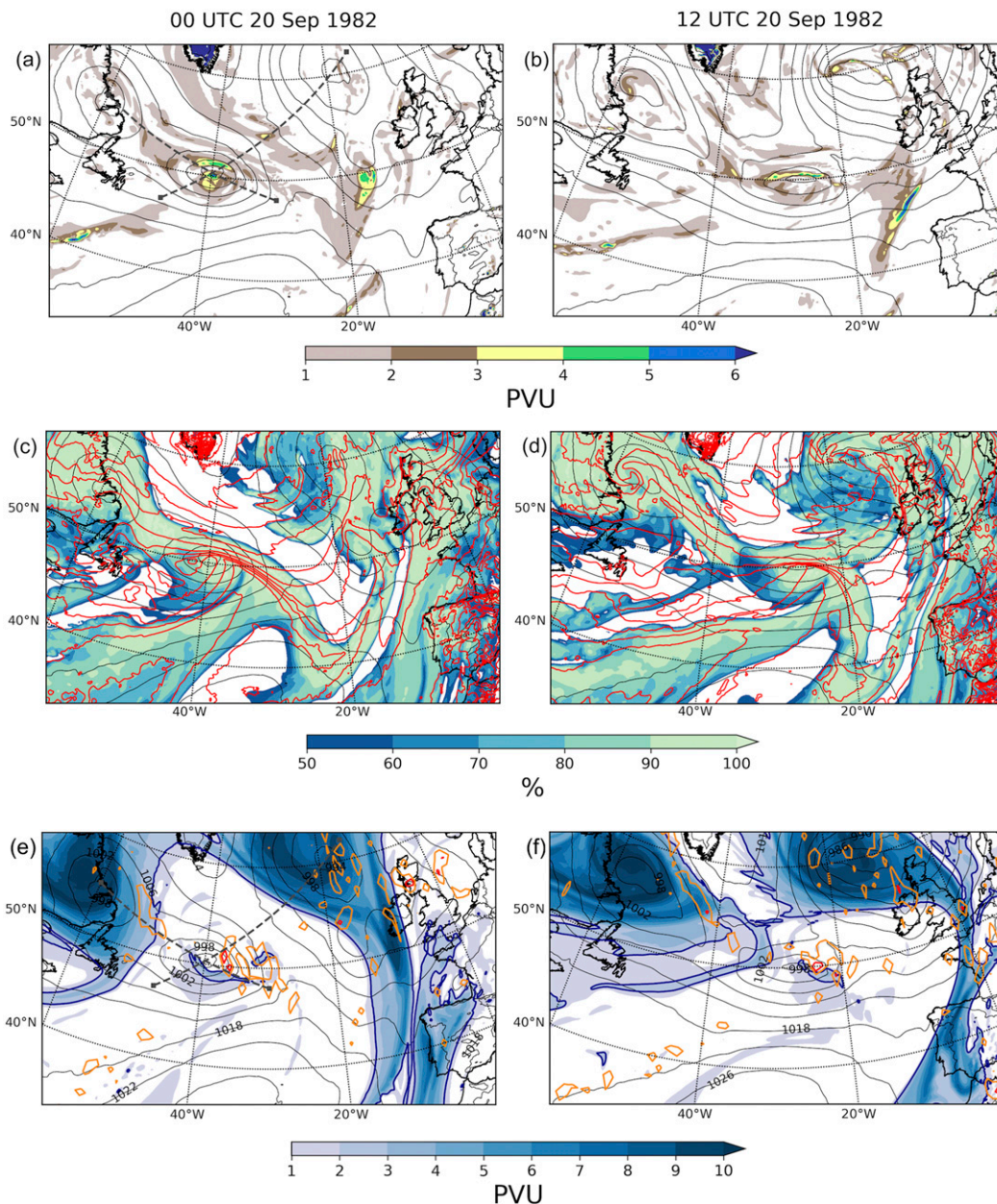
FIG. 10. OpenIFS simulation initialized on 19 Sep valid at (left) 0000 UTC 20 Sep and (right) 1200 UTC 20 Sep: (a),(b) 850-hPa potential vorticity (colors, PVU), and mean sea level pressure (black contours at 4-hPa interval). (c),(d) 850-hPa relative humidity (colors, %), 950-hPa potential temperature (red contours at 2-K interval), and mean sea level pressure (black contours at 4-hPa interval). (e),(f) 250-hPa potential vorticity (colors, 2 PVU contour also in dark blue), diabatic heating (sum of temperature tendencies from the microphysics and convection schemes) averaged over 900–700-hPa (orange contour at $0.2 \, \mathrm{K \, h^{-1}}$, red contour at $1.0 \, \mathrm{K \, h^{-1}}$), and mean sea level pressure (black contours at 4-hPa interval). Dashed lines in (a),(e) mark the locations of vertical cross sections shown in Fig. 11.

features connected directly to the low-level PV anomaly. In contrast, Fig. 10e indicates that although ex-Debby was situated beneath a large-scale ridge, there was a localized region to the south where the 250-hPa PV exceeded 2 PVU. This small-scale feature

is also evident in vertical cross sections (Fig. 11a, top-right of the panel, Fig. 11b, top-left of the panel) and is relatively close to the low-level PV anomaly of ex-Debby. For the weak upper-level forcing criterion to be met Boettcher and Wernli (2013) require that the mean
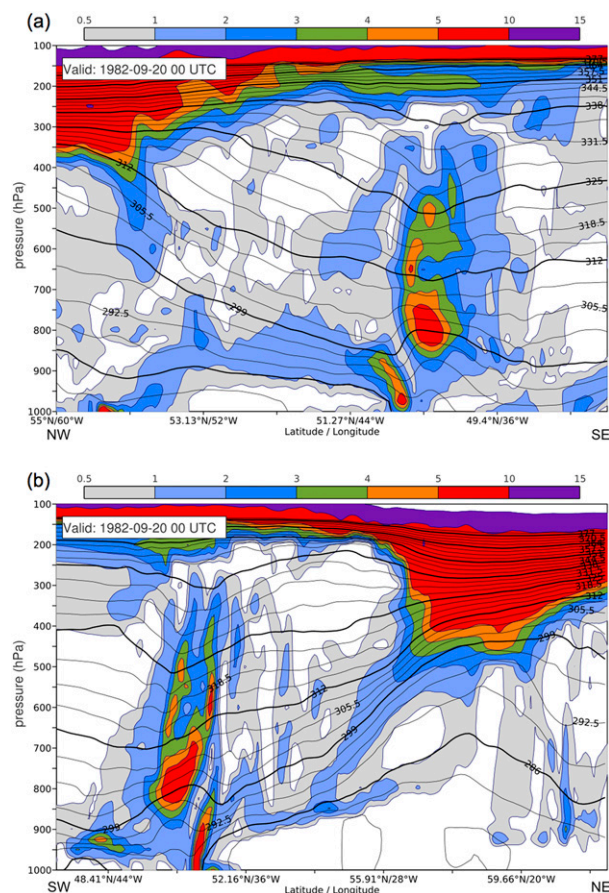
FIG. 11. Potential vorticity (colors, PVU) cross sections for the OpenIFS simulation initialized on 19 Sep valid at 0000 UTC 20 Sep: (a) (55°N, 60°W)–(48°N, 30°W), (b) (47°N, 47°W)–(62°N, 15°W). Black contours are potential temperature at 3.25-K interval.

250-hPa PV in a box that extends 4.8°E and 4.8°W, 3.6°S and 3.0°N of the cyclone center must be less than 1 PVU. Ex-Debby as simulated by OpenIFS meets this requirement between 1200 UTC 19 September and 1200 UTC 20 September but the averaged values of 250-hPa PV are close to the threshold and range from 0.89 to 0.97 PVU. Boettcher and Wernli (2013) also require that the averaged upper-level-induced quasigeostrophic ascent at 700 hPa in the same box as the PV was averaged over must be smaller than $0.5 \times 10^{-2}\,\mathrm{m\,s^{-1}}$. This diagnostic is not calculated from the OpenIFS simulation but in ERA-Interim, the upper-level-induced quasigeostrophic ascent at 700 hPa was less than $0.15 \times 10^{-2}\,\mathrm{m\,s^{-1}}$ between 1200 UTC 19 September and 1200 UTC 20 September (Maxi Boettcher, personal communication). However, the area-averaged 250-hPa PV in ERA-Interim had slightly larger values (0.89 to 1.17 PVU, Maxi Boettcher, personal communication) than in the OpenIFS simulation and was less than 1 PVU only at 1800 UTC 19 September. Ex-Debby therefore did not convincingly

meet the requirements of very weak upper-level forcing for a prolonged period of time. Thus, ex-Debby was not a classical DRW as there was some (albeit weak) upper-level forcing and also because the PV tower was deeper than observed in other DRW cases (e.g., Wernli et al. 2002; Moore et al. 2008; Boettcher and Wernli 2011). Therefore, we conclude that ex-Debby traveled rapidly across the North Atlantic as a DRW-like feature between 1200 UTC 19 September and 1200 UTC 20 September.

d. Why did ex-Debby reintensify over the United Kingdom?

ERA-Interim reanalysis showed that ex-Debby rapidly reintensified on 21 and 22 September as it moved over the south of the United Kingdom and toward Finland. To investigate the reasons for ex-Debby's reintensification over the southern United Kingdom, we analyze the model output from the OpenIFS simulation initialized on 21 September. This forecast was able to capture the track of ex-Debby and the rapid decrease in MSLP on 21 and 22 September (Fig. 7).

At 0300 UTC 21 September, ex-Debby was located south of Ireland, had a MSLP minimum of 990 hPa and a strong 850-hPa PV anomaly which exceeded 5 PVU (enlarged box in Fig. 12b). This low-level PV anomaly was small in scale but a coherent feature that was likely present in this location as a result of ex-Debby traveling across the Atlantic as a DRW-like feature. The low-level PV anomaly could constantly regenerate itself due to diabatic processes. The continued presence of the low-level positive PV anomaly is also indicative of diabatic heating in the layer above 850 hPa. At upper levels, there was a pronounced trough, which is identified from the 2-PVU contour on the 315-K isentropic surface (Fig. 12b). This is the same feature that was first identified to the east of Greenland at 0600 UTC 19 September but did not interact with ex-Debby at that time (Fig. 9a). Between 1800 UTC 19 September (Fig. 9b) and 1200 UTC 20 September (Fig. 10f), this trough moved southeast while ex-Debby moved northeast. Ex-Debby propagated eastward faster than the upper-level trough and, hence, at 0300 UTC 21 September, the surface PV anomaly of ex-Debby was located ahead (east) of the trough (Fig. 12b). Thus, at 0300 UTC 21 September this upper-level trough could interact with, and intensify, the low-level anomaly. The trough, and associated upper-level positive PV anomaly, can also be inferred from the satellite image (Fig. 6), which shows relatively clear skies over Northern Ireland and to the north.

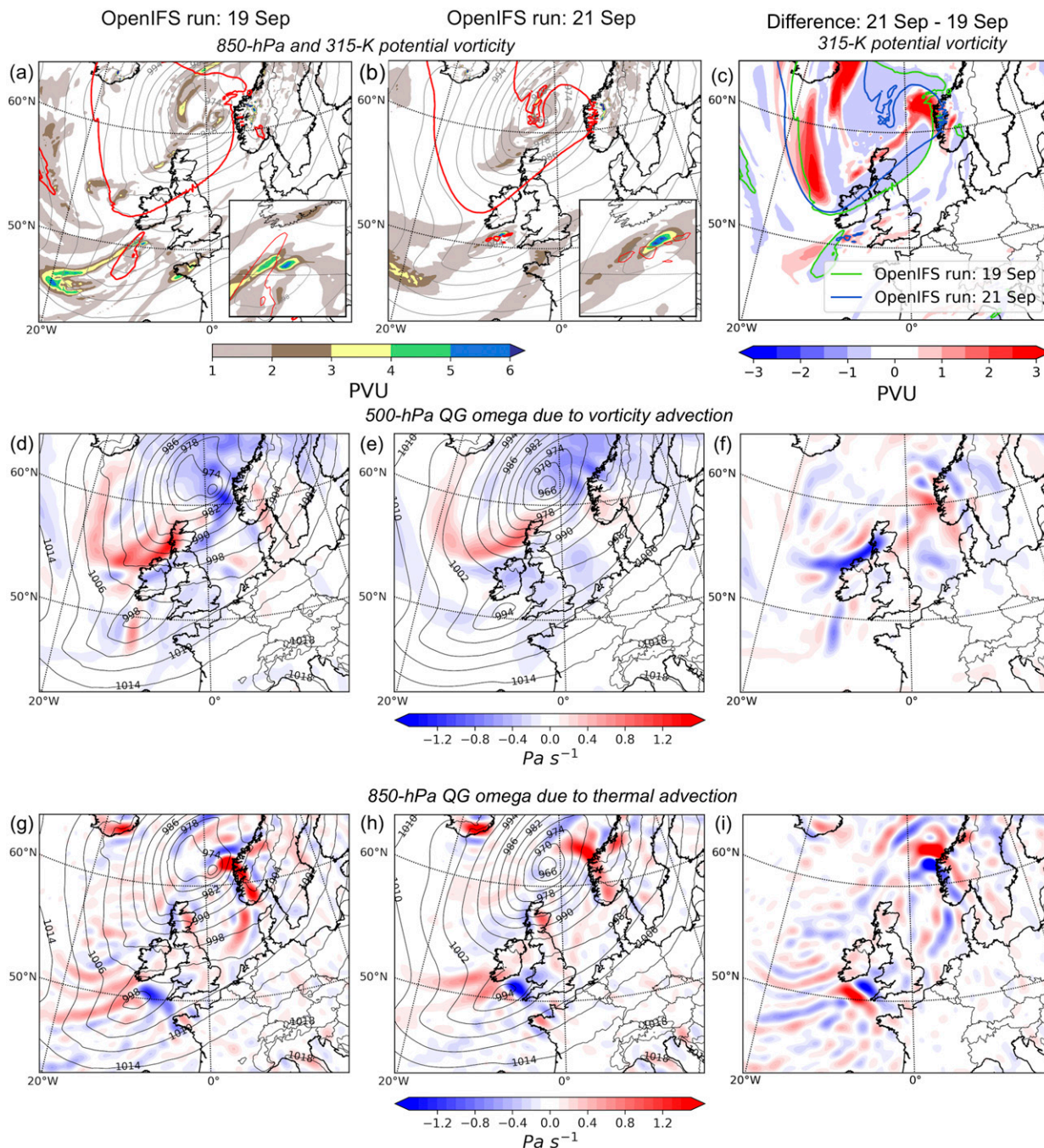Figure 12e shows that at 0300 UTC 21 September, in the OpenIFS simulation initialized on 21 September,

FIG. 12. OpenIFS simulations valid at 0300 UTC 21 Sep 1982, initialized on (left) 19 Sep, (middle) 21 Sep, and (right) the difference field 21 Sep minus 19 Sep: (a),(b) 850-hPa (colors, PVU) and 315-K (red contour at 2 PVU) potential vorticity, and mean sea level pressure (gray contours at 4-hPa interval). (c) 315-K potential vorticity at 2 PVU with 19 Sep (green contour) and 21 Sep (blue contour) simulations, and difference of 21 Sep–19 Sep (colors, PVU). (d),(e) 500-hPa quasigeostrophic omega due to vorticity advection (colors, Pa s^{-1}) and mean sea level pressure (black contours at 4-hPa interval). (f) Difference of 21 Sep–19 Sep of 500-hPa quasigeostrophic omega due to vorticity advection (colors, Pa s^{-1}). (g),(h) 850-hPa quasigeostrophic omega due to thermal advection (colors, Pa s^{-1}) and mean sea level pressure (black contours at 4-hPa interval). (i) Difference of 21 Sep–19 Sep of 850-hPa quasigeostrophic omega due to thermal advection (colors, Pa s^{-1}).

there was ascent due to vorticity advection at 500 hPa over Ireland and to the north and east of ex-Debby that had values of $-0.5\,Pa\,s^{-1}$ (approximately $5\,cm\,s^{-1}$). This suggests that relative vorticity will increase below this level in the area just north of ex-Debby [e.g., Eq. (3)]. The vertical velocity at 850 hPa due to thermal advection (Fig. 12h) shows there was strong ascent ($-1.5\,Pa\,s^{-1}$, approximately $15\,cm\,s^{-1}$) collocated and slightly downstream of ex-Debby that would also promote the intensification of the low-level cyclonic vorticity. This ascent at 850 hPa was east of the ascent at 500 hPa indicating a westward tilt with height. Finally, it should be noted that the low-level PV anomaly of ex-Debby was located in the right-hand side of the jet entrance (not shown). Thus, the rapid reintensification of ex-Debby over the United Kingdom occurred as the large-scale environment was favorable, with both warm-air and cyclonic vorticity advection present, and because the low-level and upper-level PV anomalies had now become constructively aligned, that is, the surface PV anomaly of ex-Debby was ahead of the upper-level trough, which enabled enhanced development.

To further elucidate the reasons why ex-Debby reintensified, the forecast initialized on 19 September, which did not show any reintensification (Fig. 7), is compared to the forecast from 21 September. Hence, by examining the differences between these two forecasts we can further clarify which factors likely led to the reintensification of ex-Debby.

When the left-hand column of Fig. 12 is compared to the middle column, no major differences are evident yet a number of small differences are present (difference fields are shown in the right-hand column). First, the 850-hPa PV anomaly in the forecast initialized on 19 September was weaker, less coherent, and located farther south and west than in the forecast initialized on 21 September. The 850-hPa PV values were more than 2 PVU higher in the simulation initialized on 21 September compared to the simulation initialized on 19 September (enlarged boxes in Figs. 12a and 12b). This difference suggests that more diabatic heating occurred at midlevels in the forecast initialized on 21 September, which subsequently increased the PV values below. The differences in the location, and also the strength, of the low-level PV anomaly may also result from earlier errors in the forecast when ex-Debby was simulated to travel rapidly across the Atlantic as a DRW-like feature.

The second notable difference between the two forecasts is the location of the low-level PV anomaly relative to the upper-level PV anomaly. There was a coherent positive PV anomaly on the 315-K isentrope directly above the surface anomaly in the forecast initialized on 19 September. This feature is evident as a dipole in the vertical motion due to vorticity advection (Fig. 12d). This suggests that the forecast initialized on 19 September did not predict rapid intensification of ex-Debby as the upper-level and low-level PV anomalies were already vertically stacked and thus unable to mutually enhance one another. Differences in location of the upper-level anomaly are confirmed when the red contours in Figs. 12a and 12b are considered that show that on synoptic scales the upper-level PV anomaly (associated with the trough that originated near Greenland) was farther west in the forecast initialized on 21 September compared to the forecast initialized on 19 September (Fig. 12c). This westward shift in the upper-level PV anomaly in the forecast from 21 September compared to the forecast initialized on 19 September, combined with an eastward shift in the lower-level PV anomaly, confirms that the vertical phasing differed between the two forecasts.

The third difference between the two forecasts is that the area of vertical motion due to thermal advection to the south of Ireland was shifted northeast in the simulation initialized on 21 September compared to 19 September (Figs. 12g–i). This displacement is directly related to the difference in the position of the surface low. However, the ascent due to thermal advection was stronger in the forecast from 21 September than from 19 September.

These differences discussed so far were valid at 0300 UTC 21 September, the time at which the two forecasts started to diverge. Additional times between 0600 and 1200 UTC were also considered. The ascent due to vorticity advection was further southwest and closer to ex-Debby particularly at 0600 and 0900 UTC in the forecast from 21 September (Fig. S2). This indicates that the more favorable phasing evident at 0300 UTC in the forecast from 21 September continued to exist at later times. The vertical velocity due to thermal advection is stronger at 0600, 0900, and 1200 UTC in the forecast from 21 September compared to the forecast from 19 September (Fig. S3). Furthermore, by 1200 UTC 21 September the vertical velocities due to thermal advection have started to weaken in the forecast from 19 September (Fig. S3), which demonstrates that ex-Debby weakens in this forecast due to limited coupling with upper levels.

e. What were the reasons for the strong winds over northern Finland?

On 22 September 1982, when storm Mauri traveled across northern Finland, the strongest observed 10-min average 10-m wind speeds were $23\,m\,s^{-1}$, which were recorded by three weather stations located over
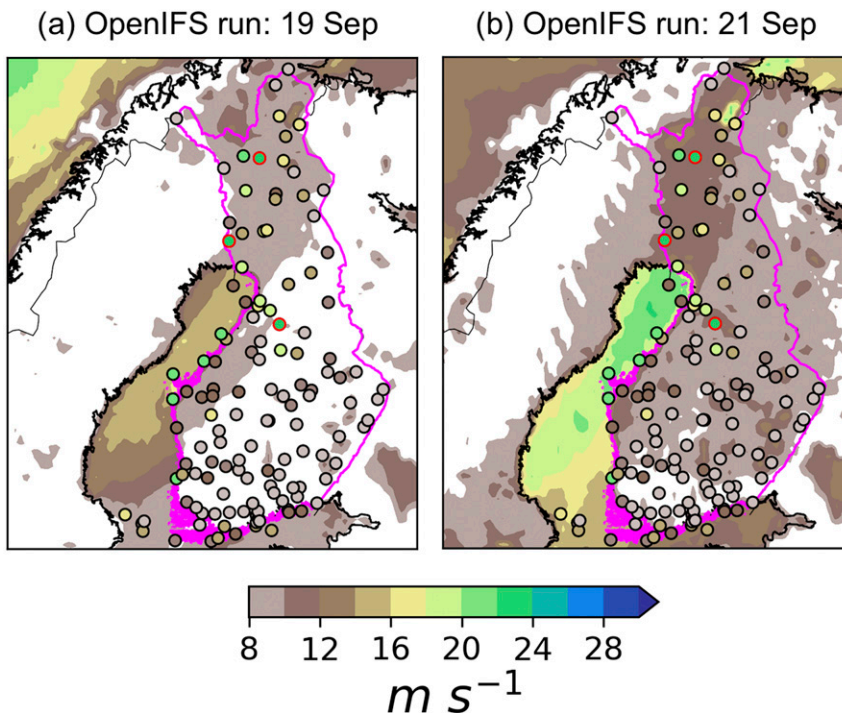
FIG. 13. Maximum observed 10-min average 10-m wind speeds during 22 Sep 1982 from Finnish Meteorological Institute's automated and manual weather stations (circles) and from OpenIFS simulations initialized on (a) 19 Sep, and (b) 21 Sep. The red circles denote the three stations that obtained the highest values of $23 \, \mathrm{m \, s^{-1}}$. Borders of Finland are colored magenta.

land in central and northern parts of Finland (Fig. 13). Nine stations in total, situated on the west coast and northern areas of Finland, observed wind speeds of $20 \, \mathrm{m \, s^{-1}}$ or more. The OpenIFS simulation initialized on 21 September shows that on 22 September the simulated 10-m wind speeds were the strongest over the Bay of Bothnia with a maximum of $22 \, \mathrm{m \, s^{-1}}$ and maximum values over land were up to $14 \, \mathrm{m \, s^{-1}}$ (Figs. 13b and 14c). There is a strong gradient in the simulated 10-m wind speeds across the coastline that is due to changes in surface roughness; in OpenIFS the surface aerodynamic roughness over sea depends on wave parameters and is typically of order $1 \times 10^{-4} \, \mathrm{m}$ whereas over land the 10-m wind speed is calculated using a surface roughness of $0.03 \, \mathrm{m}$ (see section 2c). The high winds simulated over the northern part of the Bay of Bothnia and nearby inland areas were collocated with a strong large-scale pressure gradient (Fig. 15b). When the simulated 10-m winds from the forecast initialized on 21 September are compared to the SYNOP observations from FMI (Fig. 13b), it is apparent that OpenIFS underestimates the wind speeds. The largest underestimation is over northern Finland where observed winds are $16–24 \, \mathrm{m \, s^{-1}}$ but the model simulated values are only $10–12 \, \mathrm{m \, s^{-1}}$. The

large underestimation of wind speeds in OpenIFS occurs mainly over land. Coastal locations and points near Lake Inari in the far northeast of Finland have better agreement between the observations and modeled values. Moreover, the regions of strongest modeled winds (dark brown areas in Fig. 13b) correspond well to the locations of the strongest observed winds. Hence, we can conclude that while at least over land areas the model forecast underestimates the magnitude of the wind speed it can correctly predict the location of the strongest winds.

In Finland, the volume of forest damage follows approximately a power relation as a function of wind gust speed with a power of ~10 (Valta et al. 2019). Considering European scales, it has been shown that wind gusts that exceed $35 \, \mathrm{m \, s^{-1}}$ cause the largest damages (e.g., Gardiner et al. 2013). Therefore, wind gusts are considered here in addition to the sustained wind speeds as it is likely that wind gusts were responsible for most of the damage. The 10-m wind gust, from the OpenIFS forecast initialized on 21 September, shows extremely high values reaching up to $31 \, \mathrm{m \, s^{-1}}$ over the Bay of Bothnia at 1200 UTC and also a considerable area over northern Finland where values exceed $24 \, \mathrm{m \, s^{-1}}$ (Fig. 14a). The physical reasons for the cause of
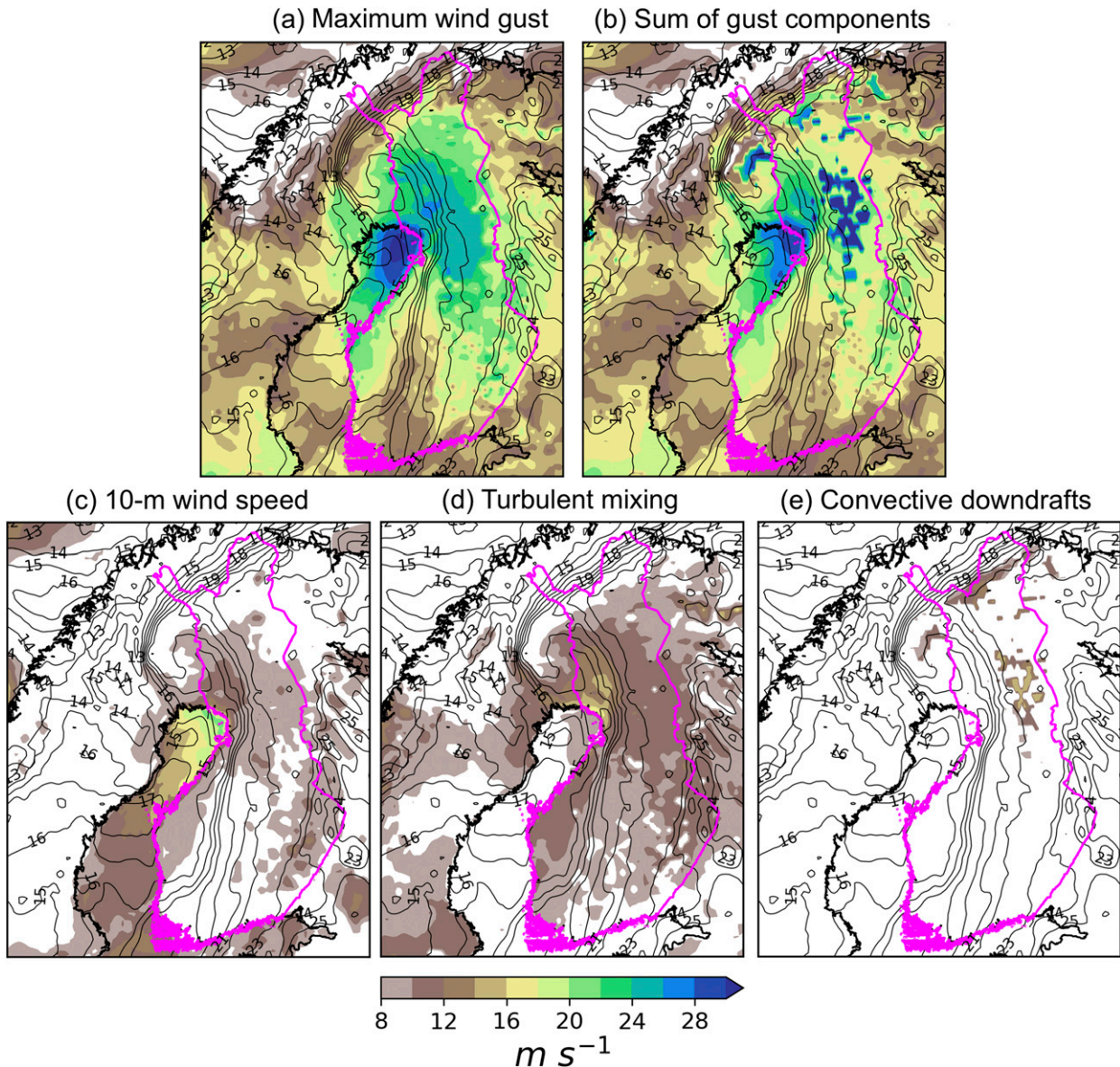
FIG. 14. OpenIFS simulation valid at 1200 UTC 22 Sep. initialized on 21 Sep. (a) Maximum 10-m wind gust (colors, m s^{-1}) in the last 1 h. (b) Sum of all wind gust components in OpenIFS gust computation. (bottom) Wind gust components: (c) 10-m wind speed, (d) turbulent mixing term, and (e) convective downdrafts term. Black contours are 850-hPa potential temperature at 1°C interval. Borders of Finland are colored magenta.

these wind gusts are now examined using the wind gust parameterization [Eq. (1)] described in section 2c as a basis. This parameterization has contributions to the total wind gust from the 10-m wind speed, turbulent mixing and convective downdrafts.

With respect to the component of the total gust due to turbulent mixing, the highest values of $18 \, \text{m s}^{-1}$ at 1200 UTC were over land behind the cold front (Fig. 14d). The location of the cold front is evident from the 850-hPa potential temperature, which shows an enhanced gradient oriented north–south in western

Finland (Fig. 14). The surface roughness generates more boundary layer turbulence over land than over sea and thus the turbulent gusts are larger over land. The turbulent gusts are also larger behind the cold front than ahead of it suggesting that the boundary layer is more unstable behind the cold front than ahead of it. This is supported by model soundings (vertical profiles—not shown), which confirm that there was a very steep lapse rate denoting an unstable boundary layer in the same location as the strongest turbulent driven gusts. This change in boundary layer
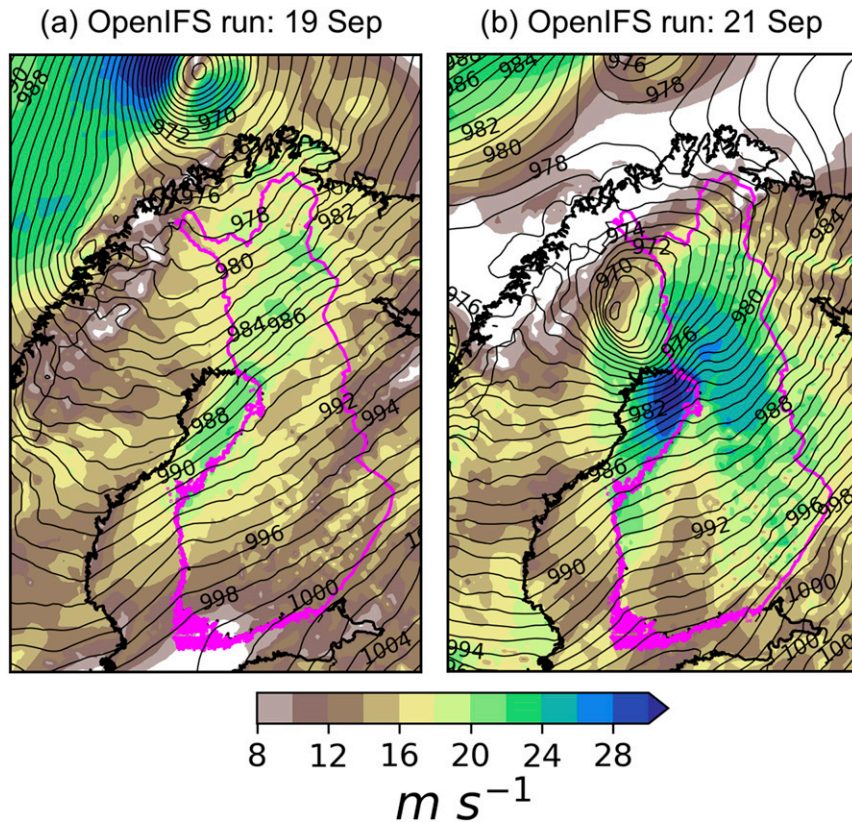
FIG. 15. Maximum 10-m wind gust (colors, m s^{-1}) during the previous hour and mean sea level pressure (contours at 1-hPa interval) at 1200 UTC 22 Sep 1982 from OpenIFS simulations initialized on (a) 19 Sep and (b) 21 Sep. Borders of Finland are colored magenta.

stability across cold fronts has been noted previously by Sinclair et al. (2010).

With respect to the 10-m wind gusts driven by convective downdrafts, the maximum values of $16 \, \mathrm{m \, s^{-1}}$ at 1200 UTC were ahead of the cold front, in the warm sector of Mauri, close to the Finnish–Russian border (Fig. 14e). In addition, there were weaker values behind the zonally extended warm front to the north. This indicates that in those regions there was strong vertical wind shear and convection present. Convective downdrafts in these regions likely induced downward mixing of high momentum air from upper levels allowing the winds reach such high values also near the surface. However, in comparison to the turbulent driven part of the 10-m wind gusts, the convective driven gusts occur in much more localized areas.

The model output gives the maximum 10-m wind gust since the previous output i.e., 1 h in this study. However, we estimated two of the three gust components from instantaneous values offline. Therefore, the sum of the three components does not exactly match with the direct model output of 10-m wind gust. By comparing Figs. 14a and 14b, we can still conclude that the patterns and magnitudes of these gusts are similar and thus the offline method can be used to identify the physical causes for the wind gusts in different regions. Three noticeable regions with elevated 10-m wind gusts were identified: 1) the Bay of Bothnia where the gusts are due to the strong large-scale pressure gradient and low surface roughness, 2) behind the cold front where turbulent mixing in an unstable boundary layer resulted in strong gusts, and 3) in the warm sector and on the warm side of the warm front where convective downdrafts likely caused the gusts.

f. What role did ex-Debby play in contributing to the strong winds?

As identified from Fig. 7, the OpenIFS forecast initialized on 21 September simulated ex-Debby to reintensify and travel to Finland whereas in the forecast initialized on 19 September ex-Debby was simulated to decay and did not travel to Fenno-Scandinavia. Therefore, by comparing these two OpenIFS forecasts, we attempt to make a first-order estimate of the possible role that ex-Debby played in the occurrence of storm Mauri and in the high winds in northern Finland.

At the time of the strongest observed winds in Finland (1200 UTC 22 September), the mean sea level pressure in both forecasts was broadly similar when only large scales are considered. Both forecasts simulated a low pressure center over the Barents Sea and a southwesterly flow over Finland (Fig. 15). However, there was one notable and critical smaller scale exception; the prominent low center of ex-Debby, which was present in the forecast initialized on 21 September was absent from MSLP pattern of the forecast from 19 September. Furthermore, there was a significant difference between the two simulations in terms of the simulated 10-m wind gust values. Although both forecasts had strong gusts, in the forecast initialized on 21 September, maximum wind gusts exceeded $31\,\mathrm{m\,s^{-1}}$ (Fig. 15b) whereas in forecast initialized on 19 September the gusts had values of up to $23\,\mathrm{m\,s^{-1}}$ (Fig. 15a). In addition, in the forecast initialized on 19 September, only a small area of land had gusts exceeding $20\,\mathrm{m\,s^{-1}}$ whereas in contrast, in the simulation from 21 September, almost all of Finland had simulated wind gusts exceeding this value (the exception being southwest inland areas). Moreover, in the forecast initialized on 21 September, there was a large area over land where the simulated wind gusts exceeded $24\,\mathrm{m\,s^{-1}}$. In addition to wind gusts, also maximum wind speeds during 22 September were $6\,\mathrm{m\,s^{-1}}$ higher over sea and $2–4\,\mathrm{m\,s^{-1}}$ higher over land in the simulation from 21 September (Fig. 13b) compared to the one from 19 September (Fig. 13a).

Storm Mauri was a high-impact storm in Finland and almost all of the impacts (e.g., felled forest) were caused by the extreme winds. Based on the comparison of the two OpenIFS forecasts, one initialized on 19 September that did not correctly capture the evolution of ex-Debby and the other on 21 September that agrees better with reanalysis and surface wind observations, it is likely that without ex-Debby the winds observed in northern Finland on 22 September 1982 would have been weaker and hence, the impacts likely would have been smaller. Thus, we conclude that ex-Debby contributed to the damaging winds but the large-scale cyclone (merged ETC1 and ETC2), and its associated upper-level trough, played a nonnegligible role.

6. Conclusions

This study investigated the extratropical transition of Hurricane Debby and the subsequent evolution of an intense extratropical windstorm, Mauri, which occurred in Finland on 22 September 1982 and led to two fatalities and extensive forest damage. The main aims were to analyze the synoptic and dynamic evolution of Debby and Mauri and to examine the causes for the strong winds over Finland.

A brief synoptic overview based on ERA-Interim reanalysis was performed before the case was analyzed in more detail using OpenIFS model simulations that had a horizontal grid spacing of 16 km. The case proved very difficult to simulate accurately. To cover the whole evolution from Debby to Mauri, with good agreement between the model forecast and ERA-Interim reanalysis, three different simulations with initialization dates on 17, 19, and 21 September were required as all three OpenIFS forecasts diverged from reanalysis after only two days. One potential reason for this could be that there were notably fewer observations in 1982 than today and thus the initial states may be less accurate than for more recent case studies. Another likely reason is that the atmospheric state was characterized by intrinsic low predictability and was strongly sensitive to the positioning and speed of certain dynamical features.

Hurricane Debby began extratropical transition on 17 September 1982, five days before the damaging winds occurred in northern Finland. At the time of extratropical transition, the upper-level waveguide was already amplified, however the divergent outflow of Debby and negative PV advection resulted in weak ridge building and an acceleration of the jet. Previous studies have noted similar evolutions, for example, Typhoon Jangmi in the Pacific also resulted in weak ridge building and jet acceleration (Grams et al. 2013). Despite the presence of a positive PV anomaly at 200 hPa immediately to the west, Debby did not reintensify immediately in the midlatitudes. This was the first critical moment in the evolution of ex-Debby. Previous studies have indicated that subsequent development and downstream modifications can be very sensitive to the phasing between the low-level PV anomaly of the tropical cyclone and the upper-level trough/PV anomaly (Riemer et al. 2008; Riboldi et al. 2019). Thus, it is possible that a very small difference in the position of Debby or in the position, intensity or phase speed of the upper-level trough could have resulted in a very different synoptic evolution over the North Atlantic.

Ex-Debby did not decay as it moved into the midlatitudes and instead retained a strong positive PV anomaly in the lower troposphere, moved into a very moist and strongly baroclinic zone, maintained a closed pressure contour and traveled rapidly east. Using the objective criteria described by Boettcher and Wernli (2013) we determined that ex-Debby evolved into a DRW-like feature and could thus maintain itself via diabatic processes as it traveled across the Atlantic. At low levels ex-Debby had all the required characteristics of a DRW but due to the presence of some (albeit weak) upper-level forcing and a PV tower we conclude that ex-Debby differs somewhat from a classical DRW.

During 19 and 20 September as ex-Debby was propagating east as a DRW-like feature, a large-scale, intense trough became evident to the east of Greenland. Initially this feature was too far north and east of ex-Debby to provide any upper-level forcing for the reintensification of ex-Debby. However, by 21 September, this upper-level PV anomaly had moved slowly east and south and had eventually become constructively aligned with ex-Debby. Ex-Debby, which was located ahead (east) of the upper-level anomaly in a region of warm-air advection and positive vorticity advection, started rapidly intensifying near the United Kingdom on 21 September. This was the second critical point in the evolution of ex-Debby. The comparison of the OpenIFS forecasts initialized on 19 and 21 September revealed that the interaction between the upper-level trough and the low-level PV anomaly of ex-Debby was important for the reintensification of ex-Debby. In the forecast initialized on 21 September, in which ex-Debby did reintensify over the southern United Kingdom, the exact locations of ex-Debby and the upper-level PV anomaly were in a favorable position to enhance the redevelopment of ex-Debby. The subsequent development of Mauri over Finland was most likely very sensitive to this phasing that was less optimal in the forecast initialized on 19 September. Furthermore, the forecast evolution was likely also heavily dependent on the intensity and coherence of the low-level PV anomaly, which was the result of the DRW-like feature. These sensitivities were apparent in the OpenIFS forecasts with differing lead times: the strong winds over Finland only became evident with a lead time of ∼2 days. To further understand the sensitivities in ex-Debby's evolution, an ensemble sensitivity analysis could be used to attain additional diagnostics.

During storm Mauri on 22 September 1982, the highest observed 10-min average 10-m wind speeds were $23\,\mathrm{m\,s^{-1}}$ over central and northern Finland. Compared to the observations, the forecast initialized on 21 September underestimates the wind speeds although the locations of the highest values are similar. Since the damage was most likely caused by strong wind gusts, we also investigated these with the forecast from 21 September. There were three distinct regions with high wind gusts. The first was over the Bay of Bothnia and was related to the strong large-scale pressure gradient and low surface roughness. The second area was behind the cold front over land where the wind gusts were primarily related to turbulent mixing in an unstable boundary layer. The third and final area of strong gusts was in the warm sector and on the warm side of the warm front where the gusts were related to convectively driven downdrafts. By comparing these

wind gusts to the forecast initialized on 19 September, in which ex-Debby did not travel to Fenno-Scandinavia, it is very likely that without ex-Debby the winds over Finland would have been weaker and that less damage would have occurred.

To conclude, this analysis has shown that storm Mauri was related to Hurricane Debby but in a complex manner: the interaction with the preexisting upper-level trough near the United Kingdom was as critical a part of Mauri's development as the occurrence of Hurricane Debby. During this critical part of the evolution of ex-Debby, the low-level PV anomaly was a small-scale feature. Such small features are particularly challenging to forecast accurately and we speculate that such anomalies, and therefore the rather unconventional way in which a damaging midlatitude windstorm Mauri evolved, may be difficult to capture in coarser-resolution models, such as climate models. This potential limitation of climate models should be considered when assessing future changes to winds and extratropical storms.

REFERENCES

Agustí-Panareda, A., C. D. Thorncroft, G. C. Craig, and S. L. Gray, 2004: The extratropical transition of Hurricane Irene (1999): A potential-vorticity perspective. *Quart. J. Roy. Meteor. Soc.*, **130**, 1047–1074, https://doi.org/10.1256/qj.02.140.

——, S. L. Gray, G. C. Craig, and C. Thorncroft, 2005: The extratropical transition of Tropical Cyclone Lili (1996) and its crucial contribution to a moderate extratropical development. *Mon. Wea. Rev.*, **133**, 1562–1573, https://doi.org/10.1175/MWR2935.1.

Archambault, H. M., L. F. Bosart, D. Keyser, and J. M. Cordeira, 2013: A climatological analysis of the extratropical flow response to recurving western North Pacific tropical cyclones. *Mon. Wea. Rev.*, **141**, 2325–2346, https://doi.org/10.1175/MWR-D-12-00257.1.

Bechtold, P., and J.-R. Bidlot, 2009: Parametrization of convective gusts. *ECMWF Newsletter*, No. 119, ECMWF, Reading, United Kingdom, 15–18, https://doi.org/10.21957/kfr42kfp8c.

Boettcher, M., and H. Wernli, 2011: Life cycle study of a diabatic Rossby wave as a precursor to rapid cyclogenesis in the North Atlantic—Dynamics and forecast performance. *Mon. Wea. Rev.*, **139**, 1861–1878, https://doi.org/10.1175/2011MWR3504.1.

——, and ——, 2013: A 10-yr climatology of diabatic Rossby waves in the Northern Hemisphere. *Mon. Wea. Rev.*, **141**, 1139–1154, https://doi.org/10.1175/MWR-D-12-00012.1.

Browning, K. A., P. Panagi, and G. Vaughan, 1998: Analysis of an ex-tropical cyclone after its reintensification as a warm-core extratropical cyclone. *Quart. J. Roy. Meteor. Soc.*, **124**, 2329–2356, https://doi.org/10.1002/qj.49712455108.

Clark, G. B., 1983: Atlantic hurricane season of 1982. *Mon. Wea. Rev.*, **111**, 1071–1079, https://doi.org/10.1175/1520-0493(1983)111<1071:AHSO>2.0.CO;2.

Dee, D. P., and Coauthors, 2011: The ERA-Interim reanalysis: Configuration and performance of the data assimilation system. *Quart. J. Roy. Meteor. Soc.*, **137**, 553–597, https://doi.org/10.1002/qj.828.

ECMWF, 2015: Subgrid-scale orographic drag. *IFS Documentation CY38R1—* Part IV: Physical processes, ECMWF, 57–65, https://www.ecmwf.int/node/9245.

——, 2019: Operational configurations of the ECMWF Integrated Forecasting System (IFS). ECMWF, accessed 15 May 2019, https://www.ecmwf.int/en/forecasts/documentation-and-support.

Evans, C., and Coauthors, 2017: The extratropical transition of tropical cyclones. Part I: Cyclone evolution and direct impacts. *Mon. Wea. Rev.*, **145**, 4317–4344, https://doi.org/10.1175/MWR-D-17-0027.1.

Galarneau, T. J., C. A. Davis, and M. A. Shapiro, 2013: Intensification of Hurricane Sandy (2012) through extratropical warm core seclusion. *Mon. Wea. Rev.*, **141**, 4296–4321, https://doi.org/10.1175/MWR-D-13-00181.1.

Gardiner, B., A. Schuck, M.-J. Schelhaas, C. Orazio, K. Blennow, and B. Nicoll, Eds., 2013: *Living with Storm Damage to Forests: What Science Can Tell Us 3*. European Forest Institute, 132 pp.

Grams, C. M., S. C. Jones, C. A. Davis, P. A. Harr, and M. Weissmann, 2013: The impact of Typhoon Jangmi (2008) on the midlatitude flow. Part I: Upper-level ridgebuilding and modification of the jet. *Quart. J. Roy. Meteor. Soc.*, **139**, 2148–2164, https://doi.org/10.1002/qj.2091.

Gregow, H., 2013: Impacts of strong winds, heavy snow loads and soil frost conditions on the risks to forests in Northern Europe. Ph.D. thesis, University of Eastern Finland, FMI Contributions 94, 44 pp. (with articles 178 pp.).

Hart, R. E., 2003: A cyclone phase space derived from thermal wind and thermal asymmetry. *Mon. Wea. Rev.*, **131**, 585–616, https://doi.org/10.1175/1520-0493(2003)131<0585:ACPSDF>2.0.CO;2.

——, and J. L. Evans, 2001: A climatology of the extratropical transition of Atlantic tropical cyclones. *J. Climate*, **14**, 546–564, https://doi.org/10.1175/1520-0442(2001)014<0546:ACOTET>2.0.CO;2.

Hewson, T. D., and U. Neu, 2015: Cyclones, windstorms and the IMILAST project. *Tellus*, **67A**, 27128, https://doi.org/10.3402/tellusa.v67.27128.

Hodges, K., A. Cobb, and P. L. Vidale, 2017: How well are tropical cyclones represented in reanalysis datasets? *J. Climate*, **30**, 5243–5264, https://doi.org/10.1175/JCLI-D-16-0557.1.

Holton, J. R., and G. J. Hakim, 2013: *An Introduction to Dynamic Meteorology*. 5th ed. Academic Press, 552 pp.

Hortal, M., 2002: The development and testing of a new two-time-level semi-Lagrangian scheme (SETTLS) in the ECMWF forecast model. *Quart. J. Roy. Meteor. Soc.*, **128**, 1671–1687, https://doi.org/10.1002/qj.200212858314.

Hoskins, B. J., and K. I. Hodges, 2002: New perspectives on the Northern Hemisphere winter storm tracks. *J. Atmos. Sci.*, **59**, 1041–1061, https://doi.org/10.1175/1520-0469(2002)059<1041:NPOTNH>2.0.CO;2.

——, M. E. McIntyre, and A. W. Robertson, 1985: On the use and significance of isentropic potential vorticity maps. *Quart. J. Roy. Meteor. Soc.*, **111**, 877–946, https://doi.org/10.1002/qj.49711147002.

Jokinen, P., H. Gregow, A. Venäläinen, and A. Laaksonen, 2014: Influence of resolution on storm studies. EGU General Assembly Conf. Abstracts, Vienna, Austria, European General Assembly, 16, 14299, https://www.egu2014.eu/.

Jones, S. C., and Coauthors, 2003: The extratropical transition of tropical cyclones: Forecast challenges, current understanding, and future directions. *Wea. Forecasting*, **18**, 1052–1092, https://doi.org/10.1175/1520-0434(2003)018<1052:TETOTC>2.0.CO;2.

Keller, J. H., and Coauthors, 2019: The extratropical transition of tropical cyclones. Part II: Interaction with the midlatitude flow, downstream impacts, and implications for predictability. *Mon. Wea. Rev.*, **147**, 1077–1106, https://doi.org/10.1175/MWR-D-17-0329.1.

Klein, P. M., P. A. Harr, and R. L. Elsberry, 2000: Extratropical transition of western North Pacific tropical cyclones: An overview and conceptual model of the transformation stage. *Wea. Forecasting*, **15**, 373–395, https://doi.org/10.1175/1520-0434(2000)015<0373:ETOWNP>2.0.CO;2.

Knapp, K. R., M. C. Kruk, D. H. Levinson, H. J. Diamond, and C. J. Neumann, 2010: The International Best Track Archive for Climate Stewardship (IBTrACS) unifying tropical cyclone data. *Bull. Amer. Meteor. Soc.*, **91**, 363–376, https://doi.org/10.1175/2009BAMS2755.1.

Laffineur, T., C. Claud, J.-P. Chaboureau, and G. Noer, 2014: Polar lows over the Nordic Seas: Improved representation in ERA-Interim compared to ERA-40 and the impact on downscaled simulations. *Mon. Wea. Rev.*, **142**, 2271–2289, https://doi.org/10.1175/MWR-D-13-00171.1.

Ma, S., H. Ritchie, J. Abraham, J. Gyakum, R. McTaggart-Cowan, and C. Fogarty, 2003: A study of the extratropical reintensification of former Hurricane Earl using Canadian Meteorological Centre regional analyses and ensemble forecasts. *Mon. Wea. Rev.*, **131**, 1342–1359, https://doi.org/10.1175/1520-0493(2003)131<1342:ASOTER>2.0.CO;2.

Moore, R. W., and M. T. Montgomery, 2004: Reexamining the dynamics of short-scale, diabatic Rossby waves and their role in midlatitude moist cyclogenesis. *J. Atmos. Sci.*, **61**, 754–768, https://doi.org/10.1175/1520-0469(2004)061<0754:RTDOSD>2.0.CO;2.

——, and ——, 2005: Analysis of an idealized, three-dimensional diabatic Rossby vortex: A coherent structure of the moist baroclinic atmosphere. *J. Atmos. Sci.*, **62**, 2703–2725, https://doi.org/10.1175/JAS3472.1.

——, ——, and H. C. Davies, 2008: The integral role of a diabatic Rossby vortex in a heavy snowfall event. *Mon. Wea. Rev.*, **136**, 1878–1897, https://doi.org/10.1175/2007MWR2257.1.

Palmén, E., 1958: Vertical circulation and release of kinetic energy during the development of Hurricane Hazel into an extratropical storm. *Tellus*, **10A**, 1–23, https://doi.org/10.1111/j.2153-3490.1958.tb01982.x.

Parker, D. J., and A. J. Thorpe, 1995: Conditional convective heating in a baroclinic atmosphere: A model of convective

frontogenesis. *J. Atmos. Sci.*, **52**, 1699–1711, https://doi.org/10.1175/1520-0469(1995)052<1699:CCHIAB>2.0.CO;2.

Pezza, A., K. Sadler, P. Uotila, T. Vihma, M. D. Mesquita, and P. Reid, 2016: Southern Hemisphere strong polar mesoscale cyclones in high-resolution datasets. *Climate Dyn.*, **47**, 1647–1660, https://doi.org/10.1007/s00382-015-2925-2.

Riboldi, J., C. M. Grams, M. Riemer, and H. M. Archambault, 2019: A phase locking perspective on Rossby wave amplification and atmospheric blocking downstream of recurving western North Pacific tropical cyclones. *Mon. Wea. Rev.*, **147**, 567–589, https://doi.org/10.1175/MWR-D-18-0271.1.

Riemer, M., and S. C. Jones, 2014: Interaction of a tropical cyclone with a high-amplitude, midlatitude wave pattern: Waviness analysis, trough deformation and track bifurcation. *Quart. J. Roy. Meteor. Soc.*, **140**, 1362–1376, https://doi.org/10.1002/qj.2221.

——, ——, and C. A. Davis, 2008: The impact of extratropical transition on the downstream flow: An idealized modelling study with a straight jet. *Quart. J. Roy. Meteor. Soc.*, **134**, 69–91, https://doi.org/10.1002/qj.189.

Ritchie, E. A., and R. L. Elsberry, 2007: Simulations of the extratropical transition of tropical cyclones: Phasing between the upper-level trough and tropical cyclones. *Mon. Wea. Rev.*, **135**, 862–876, https://doi.org/10.1175/MWR3303.1.

Ritchie, H., C. Temperton, A. Simmons, M. Hortal, T. Davies, D. Dent, and M. Hamrud, 1995: Implementation of the semi-Lagrangian method in a high-resolution version of the ECMWF forecast model. *Mon. Wea. Rev.*, **123**, 489–514, https://doi.org/10.1175/1520-0493(1995)123<0489:IOTSLM>2.0.CO;2.

Scheck, L., S. C. Jones, and M. Juckes, 2011: The resonant interaction of a tropical cyclone and a tropopause front in a barotropic model. Part II: Frontal waves. *J. Atmos. Sci.*, **68**, 420–429, https://doi.org/10.1175/2010JAS3483.1.

Schenkel, B. A., and R. E. Hart, 2012: An examination of tropical cyclone position, intensity, and intensity life cycle within atmospheric reanalysis datasets. *J. Climate*, **25**, 3453–3475, https://doi.org/10.1175/2011JCLI4208.1.

Shapiro, M. A., and D. A. Keyser, 1990: Fronts, jet streams and the tropopause. *Extratropical Cyclones: The Erik Palmén Memorial Volume*, C. W. Newton and E. O. Holopainen, Eds., Amer. Meteor. Soc., 167–191.

Sinclair, V. A., S. E. Belcher, and S. L. Gray, 2010: Synoptic controls on boundary-layer characteristics. *Bound.-Layer Meteor.*, **134**, 387–409, https://doi.org/10.1007/s10546-009-9455-6.

Staniforth, A., and J. Côté, 1991: Semi-Lagrangian integration schemes for atmospheric models—A review. *Mon. Wea. Rev.*, **119**, 2206–2223, https://doi.org/10.1175/1520-0493(1991)119<2206:SLISFA>2.0.CO;2.

Stewart, S. R., 2018: National Hurricane Center Tropical Cyclone Report: Hurricane Ophelia (9–15 October 2017). National Hurricane Center Rep. AL172017, 32 pp., https://www.nhc.noaa.gov/data/tcr/AL172017_Ophelia.pdf.

Sutcliffe, R. C., 1947: A contribution to the problem of development. *Quart. J. Roy. Meteor. Soc.*, **73**, 370–383, https://doi.org/10.1002/qj.49707331710.

Szépszó, G., and G. Carver, 2018: New forecast evaluation tool for OpenIFS. *ECMWF Newsletter*, No. 156, ECMWF, Reading, United Kingdom, 14–15, https://www.ecmwf.int/en/newsletter/156/news/new-forecast-evaluation-tool-openifs.

——, V. Sinclair, and G. Carver, 2019: Using the ECMWF OpenIFS model and state-of-the-art training techniques in meteorological education. *Adv. Sci. Res.*, **16**, 39–47, https://doi.org/10.5194/asr-16-39-2019.

Temperton, C., M. Hortal, and A. Simmons, 2001: A two-time-level semi-Lagrangian global spectral model. *Quart. J. Roy. Meteor. Soc.*, **127**, 111–127, https://doi.org/10.1002/qj.49712757107.

Thorncroft, C., and S. C. Jones, 2000: The extratropical transitions of Hurricanes Felix and Iris in 1995. *Mon. Wea. Rev.*, **128**, 947–972, https://doi.org/10.1175/1520-0493(2000)128<0947:TETOHF>2.0.CO;2.

Uotila, P., A. Pezza, J. Cassano, K. Keay, and A. Lynch, 2009: A comparison of low pressure system statistics derived from a high-resolution NWP output and three reanalysis products over the Southern Ocean. *J. Geophys. Res.*, **114**, D17105, https://doi.org/10.1029/2008JD011583.

Valta, H., I. Lehtonen, T. K. Laurila, A. Venäläinen, M. Laapas, and H. Gregow, 2019: Communicating the amount of windstorm induced forest damage by the maximum wind gust speed in Finland. *Adv. Sci. Res.*, **16**, 31–37, https://doi.org/10.5194/asr-16-31-2019.

Wernli, H., S. Dirren, M. A. Liniger, and M. Zillig, 2002: Dynamical aspects of the life cycle of the winter storm 'Lothar' (24–26 December 1999). *Quart. J. Roy. Meteor. Soc.*, **128**, 405–429, https://doi.org/10.1256/003590002321042036.

Zappa, G., L. C. Shaffrey, K. I. Hodges, P. G. Sansom, and D. B. Stephenson, 2013: A multimodel assessment of future projections of North Atlantic and European extratropical cyclones in the CMIP5 climate models. *J. Climate*, **26**, 5846–5862, https://doi.org/10.1175/JCLI-D-12-00573.1.